The Astrophysical Journal, 982:50 (29pp), 2025 March 20 https://doi.org/10.3847/1538-4357/adb3a2
© 2025. The Author(s). Published by the American Astronomical Society.
OPEN ACCESS

Empirical SED Templates for Star Clusters Observed with HST and JWST: No Strong PAH or IR Dust Emission after 5 Myr

Bradley C. Whitmore[1], Rupali Chandar[2], Janice C. Lee[1,3], Kiana F. Henny[4], M. Jimena Rodríguez[1,5], Dalya Baron[6], F. Bigiel[7], Médéric Boquien[8], Mélanie Chevance[9,10], Ryan Chown[11], Daniel A. Dale[4], Matthew Floyd[2], Kathryn Grasha[12,13], Simon C. O. Glover[9], Oleg Gnedin[14], Hamid Hassani[15], Remy Indebetouw[16], Anand Utsav Kapoor[17], Kirsten L. Larson[18], Adam K. Leroy[11], Daniel Maschmann[3,19], Fabian Scheuermann[20], Jessica Sutter[21,22], Eva Schinnerer[23], Sumit K. Sarbadhicary[11,24,25], David A. Thilker[26], Thomas G. Williams[27], and Aida Wofford[21,28]

[1] Space Telescope Science Institute, 3700 San Martin Drive, Baltimore, MD 21218, USA; whitmore@stsci.edu
[2] Ritter Astrophysical Research Center, University of Toledo, Toledo, OH 43606, USA
[3] Steward Observatory, University of Arizona, 933 N Cherry Ave, Tucson, AZ 85721, USA
[4] Department of Physics and Astronomy, University of Wyoming, Laramie, WY 82071, USA
[5] Instituto de Astrofisica de La Plata, CONICET-UNLP, Paseo del Bosque S/N, B1900FWA La Plata, Argentina
[6] The Observatories of the Carnegie Institution for Science, 813 Santa Barbara Street, Pasadena, CA 91101, USA
[7] Argelander-Institut für Astronomie, Universität Bonn, Auf dem Hügel 71, 53121, Bonn, Germany
[8] Université Côte d'Azur, Observatoire de la Côte d'Azur, CNRS, Laboratoire Lagrange, 06000, Nice, France
[9] Institut für Theoretische Astrophysik, Zentrum für Astronomie der Universität Heidelberg, Albert-Ueberle-Strasse 2, 69120 Heidelberg, Germany
[10] Cosmic Origins Of Life (COOL) Research DAO, coolresearch.io, Germany
[11] Department of Astronomy, The Ohio State University, 140 West 18th Ave., Columbus, OH 43210, USA
[12] ARC Centre of Excellence for All Sky Astrophysics in 3 Dimensions (ASTRO 3D), Australia
[13] Research School of Astronomy and Astrophysics, Australian National University, Canberra, ACT 2611, Australia
[14] Department of Astronomy, University of Michigan, Ann Arbor, MI 48109, USA
[15] Dept. of Physics, University of Alberta, 4-183 CCIS, Edmonton, Alberta, T6G 2E1, Canada
[16] University of Virginia, Charlottesville, VA, USA
[17] Sterrenkundig Observatorium, Universiteit Gent, Krijgslaan 281 S9, B-9000 Gent, Belgium
[18] AURA for the European Space Agency (ESA), Space Telescope Science Institute, 3700 San Martin Drive, Baltimore, MD 21218, USA
[19] Sorbonne Université, LERMA, Observatoire de Paris, PSL University, CNRS, F-75014, Paris, France
[20] Astronomisches Rechen-Institut, Zentrum für Astronomie der Universität Heidelberg, Mönchhofstraße 12-14, D-69120 Heidelberg, Germany
[21] Center for Astrophysics & Space Sciences, Department of Physics, University of California San Diego, 9500 Gilman Drive, La Jolla, CA 92093, USA
[22] Whitman College, 345 Boyer Avenue, Walla Walla, WA 99362, USA
[23] Max Planck Institut für Astronomie, Königstuhl 17, 69117 Heidelberg, Germany
[24] Department of Physics, The Ohio State University, Columbus, OH 43210, USA
[25] Center for Cosmology & Astro-Particle Physics, The Ohio State University, Columbus, OH 43210, USA
[26] Department of Physics and Astronomy, The Johns Hopkins University, Baltimore, MD 21218, USA
[27] Department of Physics, University of Oxford, Keble Road, Oxford OX1 3RH, UK
[28] Instituto de Astronomía, Universidad Nacional Autónoma de México, Unidad Académica en Ensenada, Km 103 Carr. Tijuana-Ensenada, Ensenada, B.C., C.P. 22860, México

Received 2024 June 23; revised 2024 December 16; accepted 2025 February 3; published 2025 March 18

Abstract

JWST observations, when combined with Hubble Space Telescope (HST) data, promise to improve age estimates of star clusters in nearby spiral galaxies. However, feedback from young cluster stars pushes out the natal gas and dust, making cluster formation and evolution a challenge to model. Here, we use JWST+ HST observations of the nearby spiral galaxy NGC 628 to produce spectral energy distribution (SED) templates of compact star clusters spanning 275 nm through 21 μm. These preliminary SEDs capture the cluster stars and associated gas and dust within radii of $\approx 0\farcs12$–$0\farcs67$ (corresponding to ≈6–33 pc at the distance of NGC 628). One important finding is that the SEDs of 1, 2, 3, and 4 Myr clusters can be differentiated in the infrared. Another is that, in 80%–90% of the cases we study, the polycyclic aromatic hydrocarbon (PAH) and H_α emission track one another, with the dust responsible for the 3.3 μm PAH emission largely removed by 4 Myr, consistent with pre-supernova stellar feedback acting quickly on the surrounding gas and dust. Nearly embedded cluster candidates have infrared SEDs that are quite similar to optically visible 1–3 Myr clusters. In nearly all cases, we find there is a young star cluster within a few tenths of an arcsec (10–30 pc) of the nearly embedded cluster, suggesting the formation of the cluster was triggered by its presence. The resulting age estimates from the empirical templates are compatible both with dynamical estimates based on CO superbubble expansion velocities, as well as the TODDLERS models, which track spherical evolution of homogeneous gas clouds around young stellar clusters.

Unified Astronomy Thesaurus concepts: Young star clusters (1833); Spiral galaxies (1560); Spectral energy distribution (2129); HST photometry (756); James Webb Space Telescope (2291); H II regions (694); Superbubbles (1656); Polycyclic aromatic hydrocarbons (1280)

Original content from this work may be used under the terms of the Creative Commons Attribution 4.0 licence. Any further distribution of this work must maintain attribution to the author(s) and the title of the work, journal citation and DOI.

1. Introduction and Motivation

Age-dating star clusters in spirals and other actively star-forming galaxies provides direct physical insight into the formation and evolution of the clusters, as well as the dynamical structures, evolution, and star formation history of the galaxy itself. The very youngest clusters, those younger than ≈3 Myr, also provide important answers to questions about the timescales for interaction between stars and the interstellar medium. Recently formed star clusters help to constrain the time it takes for giant molecular clouds to form young clusters, as well as the time it takes for stellar feedback to halt star formation (which conserves gas for future star formation) and disperse the parent cloud (A. Kawamura et al. 2009; B. C. Whitmore et al. 2014; K. Hollyhead et al. 2015; K. Grasha et al. 2018, 2019; A. M. Matthews et al. 2018; M. Chevance et al. 2020; M. Messa et al. 2021; J. A. Turner et al. 2021; J. Kim et al. 2022; J. Sun et al. 2024). However, cluster age-dating has proven to be challenging using near-ultraviolet through optical broadband photometry alone (e.g., G. Worthey 1994; B. C. Whitmore & Q. Zhang 2002; P. Anders et al. 2004; A. Wofford et al. 2016; A. Adamo et al. 2017; B. C. Whitmore et al. 2020, 2023a).

The Physics at High Angular Resolution in Nearby GalaxieS with the Hubble Space Telescope (PHANGS-HST; J. C. Lee et al. 2022, G0-15654) program has used photometric measurements in five broadband filters (NUV, *U*, *B*, *V*, and *I*) to determine the best-fit age and reddening for clusters in 38 galaxies by fitting to predictions from the G. Bruzual & S. Charlot (2003) evolutionary models (J. A. Turner et al. 2021). They found that, without additional constraints and information, such as H_α or CO, it is challenging to separate reddened young clusters from older clusters with little reddening (S. Hannon et al. 2022; B. C. Whitmore et al. 2023a; M. Floyd et al. 2024; D. Thilker et al. 2025), and there is little ability to differentiate the ages of the youngest <5 Myr clusters.

Infrared measurements of star clusters have long promised to break the well-known age–reddening degeneracy when combined with optical data, since starlight is significantly less extinguished in the infrared. Observations with JWST can capture emission from starlight (at shorter infrared wavelengths), warm ionized gas (from hydrogen recombination lines), warm dust and polycyclic aromatic hydrocarbons (PAHs) emission. Including all these components in a consistent manner is our primary challenge.

PAHs are grains that emit prominently in the mid-infrared (A. Leger & J. L. Puget 1984; J. L. Puget & A. Leger 1989; F. X. Desert et al. 1990; B. T. Draine 2003; A. Li 2020; B. T. Draine et al. 2021). The PHANGS-JWST survey (GO-2107; PI: J. Lee; J. C. Lee et al. 2023; T. G. Williams et al. 2024) includes the F335M, F770W, and F1130W filters to study PAH emission on the physical scales of star clusters. PAHs range in sizes from ∼3 to ∼100 Å, with the smallest grains emitting predominantly at 3.3 μm and being particularly sensitive to ultraviolet radiation (e.g., B. T. Draine et al. 2021; B. S. Hensley & B. T. Draine 2023). There appear to be two primary morphological signatures of PAH and IR dust emission in spiral galaxies. These have been termed "meatballs" (bright, roughly spherical, and generally in active star-forming regions) and "swiss cheese" (faint, diffuse, and generally in dust lanes) (F. Belfiore et al. 2022; A. K. Leroy et al. 2023; K. M. Sandstrom et al. 2023; D. Pathak et al. 2024; E. Schinnerer & A. K. Leroy 2024). In the current paper, we focus on the "meatball" morphology, which is generally associated with H II regions and young clusters.

The spatial resolution of a telescope varies linearly with wavelength. For this reason, early infrared (IR) studies had limited resolution, ranging from ≈5″ for IRAS (G. Neugebauer et al. 1984), to ≈2″ for SPITZER (M. W. Werner et al. 2004), to ≈5″ for Herschel (G. L. Pilbratt et al. 2010). One of the results of this limited resolution was a focus on developing SED models that were appropriate for large portions of nearby galaxies (or the entire galaxy) rather than individual star clusters. Only with the twentyfold improvement in spatial resolution offered by JWST are we now able to focus on individual star clusters in nearby spiral galaxies, and the individual parts of H II region complexes.

Most current IR SED models, such as the Code Investigation Galaxy Emission (CIGALE; M. Boquien et al. 2019) implementation of the Draine models (B. T. Draine et al. 2007) are static (rather than dynamical) models that assume "energy balance" between the radiation field (primarily in the UV) and emission from dust. While these models have been very successful for entire galaxies and kpc-scale regions in nearby galaxies that contain an integrated population containing both young, massive, UV-bright stars and the gas and dust they energize, they may not be appropriate for the study of individual star clusters on parsec scales in nearby spiral galaxies that drive outflows and typically clear the gas and dust out of the measurement aperture used to study star clusters on timescales of 2–5 Myr. Hence, the assumption of energy balance may be violated at scales that resolve star clusters.

The production of empirical spectral energy distributions (SEDs) of star clusters with independently known ages, and which cover the ultraviolet, optical, and infrared portions of the spectrum, is an important step toward accurately age-dating cluster populations in nearby galaxies. The focus of this paper is to create a new set of SEDs for star clusters that span from 275 nm through 21 μm using 14 band photometry from the PHANGS-HST and JWST programs. These can be used to age-date optically visible, partially obscured, and nearly embedded star clusters. They can also be used to help validate hydrodynamic simulations of star cluster formation (e.g., STARFORGE; M. Y. Grudić et al. 2021, 2022), as well as SED-generating simulations such as TODDLERS (A. U. Kapoor et al. 2023) or WARPFIELD-EMP (E. W. Pellegrini et al. 2020). The current paper is a pilot study that focuses on 40 star clusters in the well-studied "Phantom galaxy" NGC 628. The project will be extended in the future to include additional galaxies and to include larger cluster samples.

The rest of this paper is organized as follows. In Section 2, we summarize the JWST+HST observations, cluster catalogs and photometry, as well as the method of estimating cluster ages that is used in this work. In Section 3, we present our main results, which include the construction of new empirical template SEDs for star clusters. In Section 4, we compare our empirical SEDs with predictions from the TODDLERS (A. U. Kapoor et al. 2023) SED model suite, and discuss previous observational work in the context of our new cluster templates. We summarize our main results and discuss future work in Section 5.

2. Data and Cluster Training Sets

2.1. HST and JWST Observations and Cluster Catalogs

In this work, we use photometry of clusters in NGC 628 in 14 filters, which cover wavelengths from 0.275 to 21 μm, performed on HST+JWST images. NGC 628, also known as the Phantom galaxy, is a nearly face-on, grand-design spiral galaxy at a distance of 9.84 $\pm$ 0.63 Mpc (G. S. Anand et al. 2021). It has been the focus of several studies made by the PHANGS collaboration, as well as the LEGUS (D. Calzetti et al. 2015) and FEAST (B. Gregg et al. 2024; A. Adamo et al. 2025, in preparation) projects. Figure 1 shows a *B*, *V*, H_α color image of NGC 628, highlighting the H II regions strung along the spiral arms in red (H_α). Figure 2 shows a *B*, *V*, 7.7 μm color image where the PAH emission (red) traces both H_α and also the diffuse dust lanes. A careful comparison of Figures 1 and 2 shows that, in most cases, the regions with strong 7.7 μm emission also have strong H_α emission, a result that is established more quantitatively in H. Hassani et al. (2023).

NGC 628 was observed in five bands by HST (WFC3/F275W, WFC3/336W, ACS/F435W, ACS/555W, and ACS/F814W) as part of the LEGUS survey (D. Calzetti et al. 2015), and was reduced using the PHANGS-HST pipeline (see J. C. Lee et al. 2022 for more details). Narrowband observations of the H_α line taken with the ACS/F658N filter (Proposal 10402, PI: Chandar, R. Chandar et al. 2025) also exist in the archive. See J. C. Lee et al. (2022)[29] for details about PHANGS-HST. The Advanced Camera for Surveys (ACS) data was drizzled onto a WFC3-like grid, using GAIA (Gaia Collaboration et al. 2016) stars for the alignment. The pixel scale of 0.″0396 for WFC3 pixels corresponds to 1.890 pc pix^{-1} at the assumed distance of 9.84 Mpc for NGC 628.

JWST observations of NGC 628 are available in the F200W, F300M, F335M, and F360M NIRCAM filters and in the F770W, F1000W, F1130W, and F2100W MIRI fiiters, as part of a Cycle 1 JWST Treasury program (proposal 2107; PI: J. Lee; J. C. Lee et al. 2023). See J. C. Lee et al. (2023) and T. G. Williams et al. (2024) for additional details about the observations and basic reductions.

In this work, we start from the PHANGS-HST catalog of compact star clusters (B. C. Whitmore et al. 2021; D. A. Thilker et al. 2022; D. Maschmann et al. 2024). ID numbers for the optically selected star clusters used in this paper are from D. Maschmann et al. (2024). Clusters were selected to be extended sources that are broader than the PSF based on measurements of multiple concentration indices (D. A. Thilker et al. 2022). The extended sources in these initial catalogs were then classified by visual inspection by author B. Whitmore (human classification) and by machine learning algorithms into Class 1 (single-peaked, symmetric clusters), Class 2 (single-peaked, asymmetric clusters), Class 3 (multiply peaked, compact associations) and Class 4 (contaminants) (W. Wei et al. 2020; B. C. Whitmore et al. 2021; S. Hannon et al. 2023). In this work, we use the 489 human-classified Class 1 + 2 catalog in NGC 628. However, the number of clusters used in different parts of the analysis is smaller for a variety of reasons, including being faint (often in the UV) or missing due to a somewhat different field of view (primarily JWST filters). Of the 489 clusters, only 291 have $U-B$, $V-I$, *I*–3.3 μm, and 3.0–7.7 μm measurements required to include the cluster in various parts of the analysis performed in this paper.

[29] https://archive.stsci.edu/hlsp/phangs

2.2. Photometry

2.2.1. Small- versus Large-aperture Photometry

The difference in spatial resolution as a function of wavelength (e.g., effective radius of a PSF $\approx$ 0.″08 for the F555W filter and $\approx$0.″67 for the F2100W filter) provides an important and difficult challenge for multiwavelength studies of star clusters. A common approach is to convolve the shorter-wavelength images to have comparable resolution to the longer-wavelength images, so that the apertures are effectively "matched." While this approach gives up some spatial resolution information, it gains a degree of uniformity in at least attempting to look at the same objects and field of view.

In our case, we are primarily interested in the star clusters, which are barely resolved and often very close together. Hence, spatial resolution is our primary concern and we therefore use "small-aperture" photometry as our primary method in most of this paper. In addition, it is not always possible to "look at the same objects," even when matching the field of view with convolved images and larger apertures. This is because the IR flux for the youngest regions (1–5 Myr) is generally dominated by emission from gas and dust (i.e., thermal dust continuum, PAH emission, warm ionized gas), while optical flux is dominated by stellar-continuum emission. Hence, although the stellar light stays in one place and is observed in both the optical and IR, the gas and dust associated with the cluster generally expands to sizes that are many times larger than even the large 0.″67 radius of the F2100W PSF in just a few Myr. Hence, it is not possible to actually match the features associated with young clusters at all ages.

In Section 3.2 and Appendix B, we return to this topic by making a comparison between small-aperture photometry and photometry based on images convolved to the resolution of the 21 μm image based on the paper by H. Hassani et al. (2023). This provides more quantitative information comparing the two approaches to performing photometry. Luckily, the dynamic situation responsible for this problem also provides the solution for our age-dating goals, since it removes the gas and dust from the aperture in only a few million years, resulting in fluxes that vary by a factor of more than a hundred in the F2100W filter in roughly five Myr.

2.2.2. Photometric Parameters

Typically, an aperture radius of 0.″1–0.″2 (i.e., 3 to 5 ACS or WFC3 pixels using HST; $\approx$5–10 pc for galaxies at 10 Mpc) has been used to study star clusters in nearby galaxies (e.g., R. Chandar et al. 2010; B. C. Whitmore et al. 2010; N. Bastian et al. 2012; A. Adamo et al. 2017). This allows studies to focus on a single star cluster in regions that are often very crowded, while still excluding neighboring clusters and stars. In principle, we could use much larger radii that cover the entire H II complex, often several hundred pc in size. However, this would result in the inclusion of several (or even dozens) of nearby star clusters covering a wide range of ages, thus defeating the basic aim of the project, which is to study the ages and evolution of individual clusters.

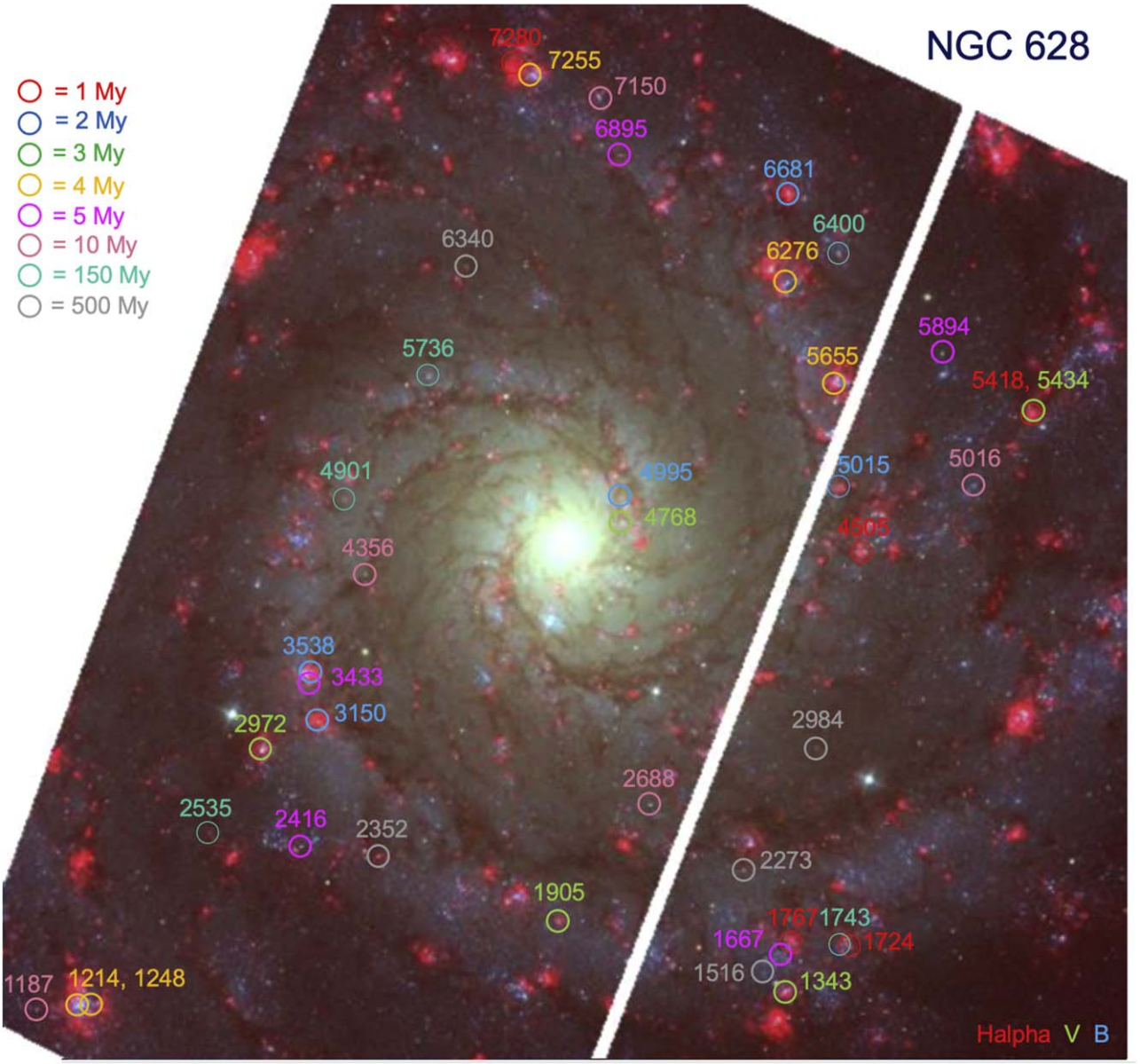

Figure 1. Hα, *V*, *B* HST image of a portion of NGC 628 showing the locations of star clusters in our training set of Class 1 and 2 PHANGS-HST clusters for building our empirical SED templates. The color-coded adopted ages, derived as explained in Section 2.3.1, are marked by circles, with the ID numbers from the human-classified compact cluster catalog included. Close-up snapshots of the clusters are included in Figures 5 and 6.

For the current paper, our primary method of performing photometry uses small apertures centered on the clusters in the HST observations. More specifically, a 4 WFC3-pixel (0.″158) radius with a sky annulus from 7 to 8 WFC3 pixels, and aperture corrections based on bright isolated star clusters (see S. Deger et al. 2022 for details). We note that there are small (typically a few hundredths of a magnitude) differences between the HST photometry used in the current paper (from M. Rodríguez et al. 2025) when compared to the original photometry in J. A. Turner et al. (2021), due to the use of different software packages.

The spatial resolution in NIRCAM bands is similar to HST, hence comparable 4 pixel (0.″124) radii apertures were employed with a sky annulus from 7 to 8 NIRCAM pixels. Aperture corrections were derived based on bright isolated globular clusters in NGC 628.

Aperture photometry for the MIRI observations used the 50% encircled energy radii for stars. A sky annulus of 13–14 MIRI pixels (1.″43 and 1.″54) is used in all MIRI bands. The total brightness is then obtained by doubling the measured flux, since the clusters are essentially point sources in the MIRI bands. See M. Rodríguez et al. (2025) for details about the HST, NIRCAM, and MIRI photometry used in the current paper. This is referred to as "small-aperture photometry" throughout this paper.

It should be noted that, while the aperture corrections are reasonable for the star clusters themselves, they are largely meaningless for the interstellar medium (ISM) components associated with very young clusters, due to the rapid expansion of the superbubbles. Fortunately, as we will see in Section 3, there is a factor of ∼100 difference between the flux of a 1 and a 5 Myr cluster in the MIRI bands, significantly larger than the uncertainties in the aperture corrections.

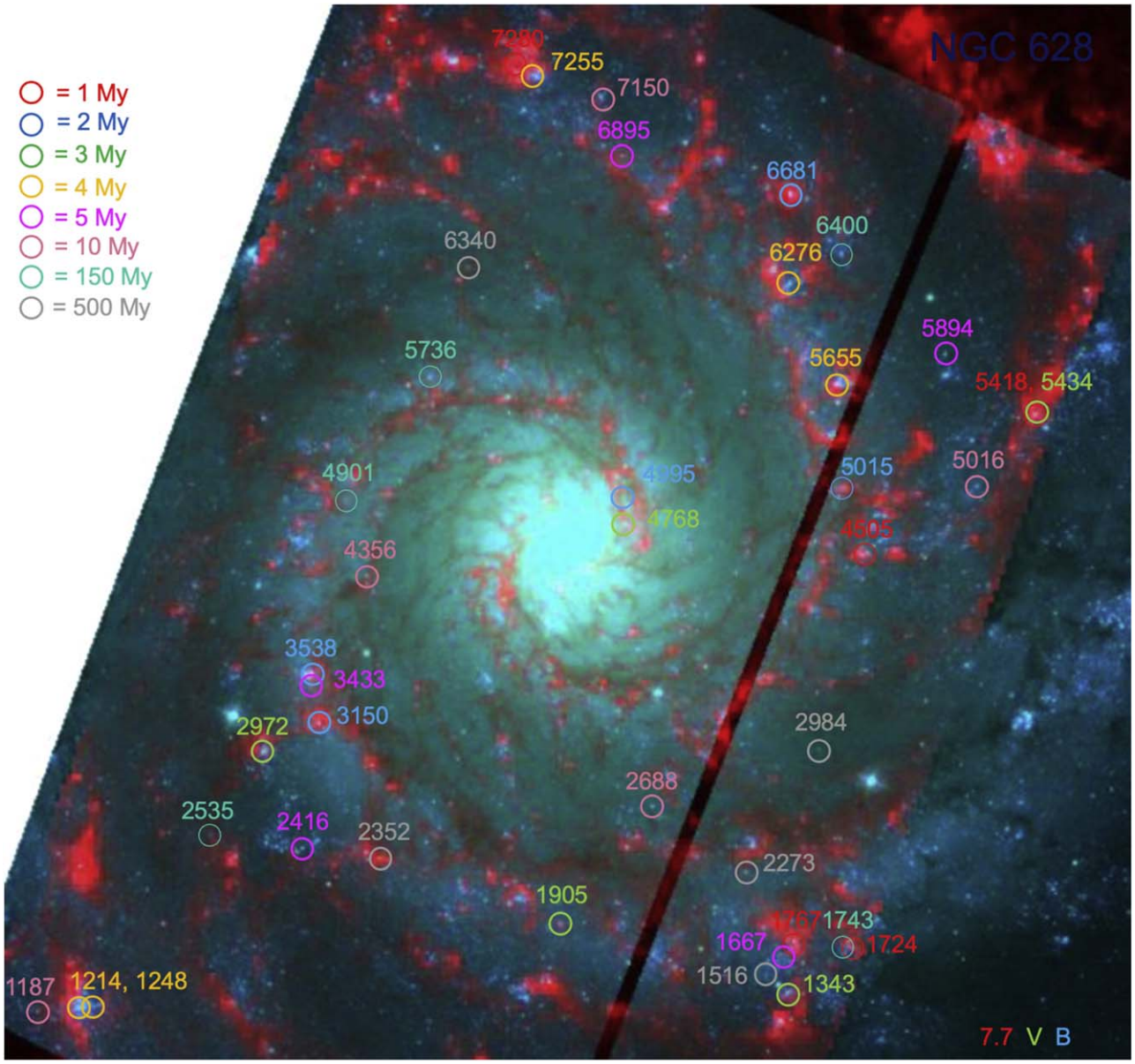

Figure 2. 7.7 μm (JWST), *V*, *B* image of the same region as shown in Figure 1, with the same labeling. Note that the bottom right portion of the image was not covered by the JWST observations, limiting the region of NGC 628 that could be used to define the training set.

Fluxes are measured/converted into Jansky for all filters. When only optical colors are presented, they are converted to the VEGAMAG system[30] (for example, in Section 2.3.1 and Figure 3), and when HST and JWST colors are plotted together, all filters are in the ABMAG system (for example, in Section 3.4).

As discussed in Sections 2.2.1, 3.2, and Appendix B, we also perform convolved large-aperture photometry and compare it with our results using small-aperture photometry for some aspects of the analysis. Briefly, this uses ASTRODENDRO (T. Robitaille et al. 2019) to identify sources in the F2100W image, and then measures fluxes at these locations on images of the various filters that have been convolved to the same spatial resolution as the F2100W image (i.e., 0.″67). A background is subtracted using median values in an annulus that is 2–3 times larger than the F2100W resolution (i.e., 1.″34–2.″01). See H. Hassani et al. (2023) for details.

The photometry used in the current paper is the version available in summer 2024 from the various studies listed above. Later versions of the photometry may vary, generally slightly. For this reason, the photometry is included in the tables of the current paper.

2.3. Cluster Age Estimates

In this section, we start with class 1+2 clusters identified in the human-classified PHANGS-HST catalog (see D. Maschmann et al. 2024 for details). We use two independent associated methods to estimates ages, both independent of the normal PHANGS SED age estimates reported in J. A. Turner et al. (2021), K. F. Henny et al. (2025), and D. Thilker et al. (2025).[31]

[30] The VEGAMAG system has been used in most past studies that have focused on optical observations. The use of VEGAMAG for these particular figures is designed to facilitate comparison to previous results such as R. Chandar et al. (2010) and A. Adamo et al. (2017).

[31] In principle, we could use ages determined by these other methods, but while most of these ages are robust, there are some remaining biases as well.

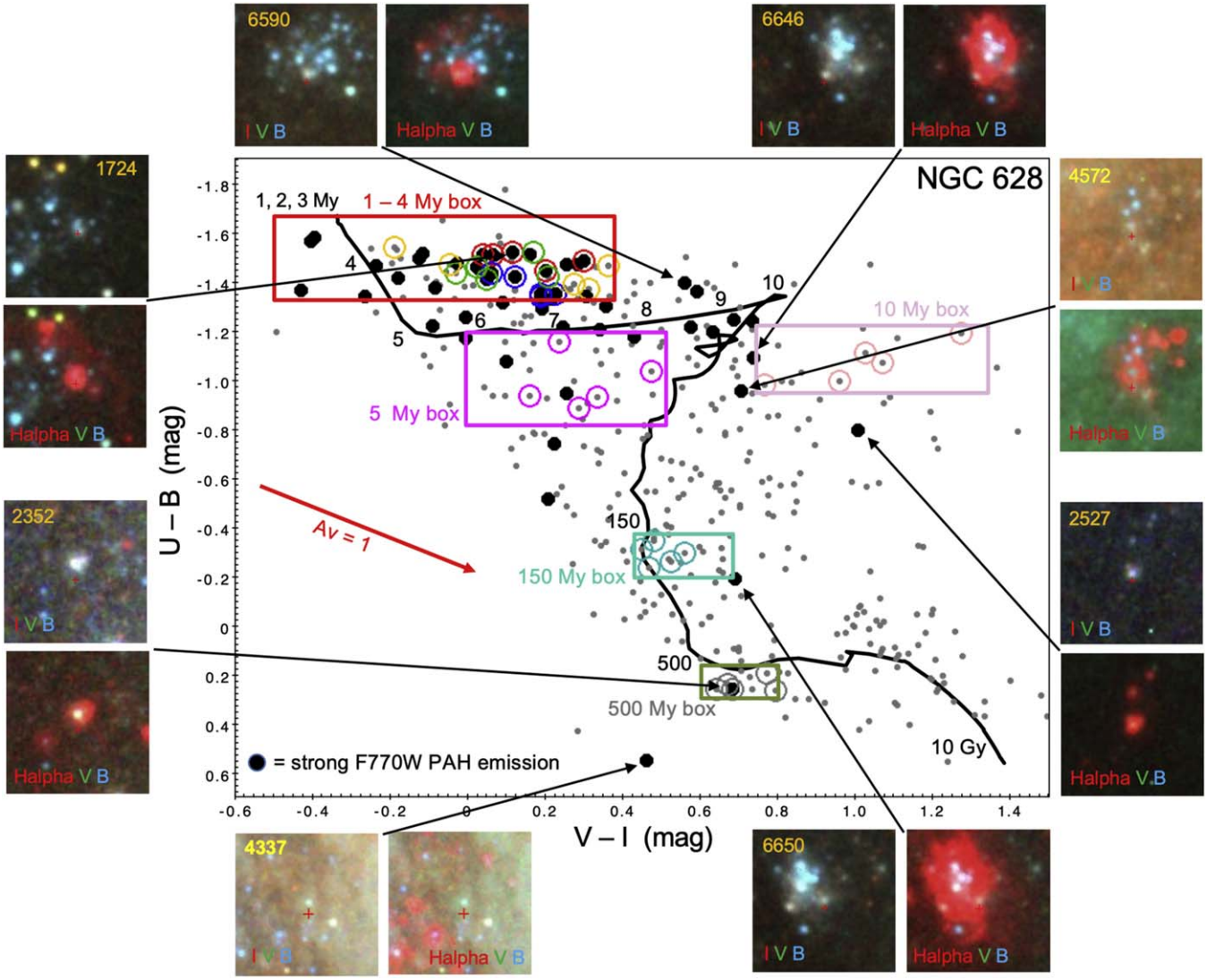

Figure 3. $U-B$ vs. $V-I$ diagram with the five "degeneracy-free" regions shown, as discussed in the text. The clusters from the training set are identified using color-coded circles defined in Figure 1. Clusters with strong PAH emission (i.e., F770W/F300M > 20) are shown in black. Most of these clusters with strong PAHS are above the 10 Myr position, as determined by the BC03 models shown by the black line, and are compatible with being from the 1 to 4 Myr box with varying degrees of reddening. Five of the six clusters that are potentially older than 10 Myr have strong H_α emission, as shown by the snapshots, and hence are young clusters (1–5 Myr) with $A_V \approx 1.2$–2.5 mag. Hence, from this figure alone, it is clear that nearly all strong PAH emitters have ages less than about 5 Myr.

The first method relies on specific ranges of $U-B$ and $V-I$ colors that uniquely establish the ages of the clusters rather than being affected by the age/reddening/metallicity degeneracies. This is possible for clusters with ages of ≈1–4, 5, 10, 150, and 500 Myr, which can then be used as a "skeleton" to build templates at all ages.

The second method uses the size of H_α superbubbles around very young clusters to approximately refine cluster ages of 1, 2, 3, and 4 Myr (see B. C. Whitmore et al. 2011; S. Hannon et al. 2022; A. Pedrini et al. 2024). We select the five most massive clusters (generally $> 3000\,M_{\rm solar}$) at each age to minimize the impact of stochasticity on the integrated flux measurements (e.g., M. Fouesneau & A. Lançon 2010; M. Fouesneau et al. 2012; M. R. Krumholz et al. 2015; A. Wofford et al. 2016; S. Hannon et al. 2019; B. C. Whitmore et al. 2020; J. A. Turner et al. 2021). The locations of these clusters are shown in Figures 1 and 2.

2.3.1. *Initial Age Estimates from Degeneracy-free Regions in the* U − B *versus* V − I *Color–Color Diagram*

Figure 3 shows a $U-B$ versus $V-I$ color–color diagram for star clusters in NGC 628. This diagram is the workhorse for several PHANGS-HST studies; the reader is referred to papers from the PHANGS collaboration (e.g., J. A. Turner et al. 2021; B. C. Whitmore et al. 2021; S. Deger et al. 2022; D. Maschmann et al. 2024), as well as earlier papers such as B. C. Whitmore & Q. Zhang (2002), R. Chandar et al. (2010), and A. Adamo et al. (2017) for details. While the degeneracy between age and reddening in broadband colors can make it challenging to estimate the ages of clusters in many parts of this diagram (P. Anders et al. 2004; B. C. Whitmore & Q. Zhang 2002; B. C. Whitmore et al. 2023a; D. Thilker et al. 2025), there are regions in the color–color diagram where clusters can generally only have a single age or very small range of ages. We will refer to these as "degeneracy-free

Table 1
Properties of the Cluster Training Sample Used to Make Empirical SED Templates

	ID[a]	Adp. Age[b] (Myr)	$R^{c}_{H\alpha}$ (pix)	R.A. (deg)	Decl. (deg)	SEDFIX Age[d] (Myr)	log M[d] ($M_{\odot}$)	EBV[a,e] (mag)	$U-B$[e] (mag)	$V-I$[e] (mag)	I-3.3[f] (mag)	3.0–7.7[f] (mag)
1	1724	1.0	0	24.160755	15.765572	2.0	3.49	0.26	−1.52	0.12	1.07	4.29
2	1767	1.0	0	24.163475	15.765885	2.0	4.07	0.22	−1.49	0.30	0.91	4.30
3	4505	1.0	0	24.160275	15.783140	2.0	3.62	0.10	−1.45	0.20	−0.10	4.45
4	5418	1.0	0	24.152300	15.789327	3.0	3.75	0.18	−1.51	0.04	0.24	4.24
5	7280	1.0	0	24.176468	15.804831	3.0	3.53	0.14	−1.51	0.07	0.42	4.69
6	3150	2.0	2	24.185388	15.775613	3.0	4.08	0.24	−1.34	0.19	−0.80	4.77
7	3538	2.0	2	24.185787	15.777906	3.0	3.83	0.18	−1.44	0.06	−0.02	3.93
8	4995	2.0	1	24.171566	15.786123	3.0	3.41	0.20	−1.35	0.23	−0.17	4.83
9	5015	2.0	2	24.161094	15.786205	3.0	3.51	0.20	−1.35	0.19	−0.01	3.70
10	6681	2.0	1	24.163612	15.799347	3.0	3.78	0.14	−1.42	0.12	−0.42	4.77
11	1905	3.0	3	24.174276	15.766726	3.0	3.39	0.10	−1.41	0.05	−0.99	4.48
12	1343	3.0	4	24.163696	15.763633	1.0	4.26	0.22	−1.43	0.21	−1.81	−1.07
13	2972	3.0	4	24.187976	15.774374	3.0	4.22	0.10	−1.44	−0.03	−1.71	2.31
14	4768	3.1	2	24.171274	15.784595	2.0	3.75	0.16	−1.52	0.17	−0.99	0.97
15	5434	3.0	3	24.152246	15.789426	3.0	3.69	0.18	−1.46	0.02	−1.78	4.60
16	1214	4.0	12	24.196543	15.762902	7.0[g]	3.99[g]	0.01[g]	−1.37	0.31	0.4	−0.20
17	1248	4.0	5	24.195676	15.763044	3.0[g]	3.60[g]	0.03[g]	−1.54	−0.19	−3.14	1.24
18	5655	4.0	5	24.161463	15.790765	3.0	4.05	0.14	−1.47	−0.05	−2.06	3.23
19	6276	4.0	17	24.163632	15.795263	1.0	4.68	0.24	−1.39	0.27	−0.09	−0.85
20	7255	4.1	17	24.175683	15.804612	1.0	3.72	0.26	−1.47	0.36	−3.85	1.98
21	1667	5.0	5	24.164027	15.765316	1.0	3.84	0.34	−1.16	0.23	−2.32	2.55
22	2416	5.0	20	24.186201	15.770045	8.0	4.02	0.16	−1.04	0.47	−0.21	−1.91
23	3433	5.0	6	24.185832	15.777333	5.0	3.61	0.28	−0.94	0.16	−1.42	2.31
24	5894	5.0	−999	24.156443	15.792100	7.0	3.70	0.14	−0.93	0.33	−1.3	−1.72
25	6895	5.0	−999	24.171399	15.800950	4.0	3.74	0.46	−0.89	0.29	−3.06	0.53
26	1187	10.0	−999	24.198491	15.762762	9.0[g]	4.07[g]	0.38[g]	−1.0	0.96	−0.69	−0.95
27	2688	10.0	−999	24.169986	15.771925	10.0	4.07	0.12	−1.11	1.03	−0.43	−1.76
28	4356	10.0	−999	24.183245	15.782235	10.0	3.67	0.18	−1.19	1.27	0.19	−2.74
29	5016	10.0	−999	24.154924	15.786206	10.0	3.90	0.14	−1.07	1.07	−0.43	−3.76
30	7150	10.0	26	24.172343	15.803480	8.0	3.82	0.34	−0.98	0.76	−1.71	1.61
31	1743	150.0	15	24.161103	15.765697	124.0	4.04	0.10	−0.30	0.56	−3.42	0.90
32	2535	150.0	14	24.190482	15.770641	175.0	4.01	0.04	−0.31	0.45	−1.70	1.74
33	4901	150.0	−999	24.184198	15.785612	175.0	4.03	0.06	−0.35	0.48	−1.52	−0.29
34	5736	150.0	−999	24.180184	15.791151	197.0	3.98	0.02	−0.26	0.52	−1.70	−0.33
35	6400	150.0	6	24.161230	15.796543	156.0	4.33	0.00	−0.24	0.47	−1.33	−2.05
36	1516	500.0	−999	24.164762	15.764410	311.0	4.11	0.04	0.24	0.67	0.53	−1.13
37	2273	500.0	−999	24.165669	15.768983	391.0	4.57	0.06	0.26	0.64	−1.38	0.94
38	2352	500.1	3	24.182627	15.769619	5.0	4.34	0.96	0.26	0.68	−0.60	3.45
39	2984	500.0	−999	24.162251	15.774448	874.0	4.48	0.08	0.26	0.80	−1.29	−2.02
40	6340	500.0	−999	24.178579	15.796022	695.0	4.39	0.00	0.19	0.77	−0.23	−0.72

Notes.
[a] Star Cluster ID # from D. Maschmann et al. (2024).
[b] Adopted age as discussed in Sections 2.3. The values with "0.1" attached are the outliers discussed in Section 2.5.
[c] Distance in HST pixels from star cluster to the nearest H_{α} feature., which may or may not be associated with the star cluster in the older objects. Values of −999 are used when there is no H_{α} present in the snapshot.
[d] The SED-TreeFit (SEDFIX in heading) age, mass, and $E(B-V)$ reddening estimates based on HST observations from D. Thilker et al. (2025).
[e] Values in VEGAmag.
[f] Values in ABmag.
[g] From J. A. Turner et al. (2021), since ages for these objects are missing in D. Thilker et al. (2025).

regions," and the associated ages will be referred to as "adopted" ages. These regions are identified by the boxes in Figure 3.

The box containing clusters with ages between 1 and 4 Myr is shown in red and is the clearest example of a specific region in color–color space that is not very sensitive to the age–reddening degeneracy. The colors in this box are consistent with colors predicted by the G. Bruzual & S. Charlot (2003, hereafter BC03) solar-metallicity models for 1, 2, 3, and 4 Myr star clusters, with a small to moderate amount of reddening added (i.e., $E(B-V)=0.1$–0.3 mag, hence $A_V \approx 0.3$–0.9 mag). These clusters are blueward in the $U-B$ of the horizontal portion of the BC03 model line expected for 5–10 Myr clusters, when red supergiants (RSGs) start to appear (see Figure 3). Hence the clusters would require a negative (nonphysical) value of A_V to reach positions from the BC03 models with ages 6–9 Myr. A visual examination of all clusters in the 1–4 Myr box shows that most have strong H_{α} emission, as expected for very young clusters. We take a closer look at the clusters in the 1–4 Myr box in Appendix A.

Table 1 shows that all the clusters in the 1–4 Myr box with measured age estimates using the SED-TreeFit approach from

D. Thilker et al. 2025 have ages less than 4 Myr. This provides an independent sanity check that all of the clusters in the 1–4 Myr box are likely to be very young.

Similar degeneracy-free regions in the $U-B$ versus $V-I$ color–color diagram are identified for 4–7 Myr (maroon—5 Myr box), 9–11 Myr (gold—10 Myr box), 100–250 Myr (cyan—150 Myr box), and 300–800 Myr (gray—500 Myr box). In all these cases, backtracking along the reddening vector (toward the upper left) intersects the solar-metallicity BC03 model in a very small range of ages, hence minimizing degeneracies and providing more certain age estimates. This is not true for many other regions of the $U-B$ versus $V-I$ color–color diagram. For example, an old globular cluster can be assigned an age of 13 Gyr, 1 Gyr, 100 Myr, 6 Myr, or 1 Myr, depending on how much reddening is assigned (see B. C. Whitmore et al. 2023a; D. Thilker et al. 2025).

While different stellar evolutionary models, such as GALEV, Yggdrasil, STARBURST99, and BC03 (C. Leitherer et al. 2002; G. Bruzual & S. Charlot 2003; R. Kotulla et al. 2009; E. Zackrisson et al. 2011) make somewhat different predictions for the evolution of $U-B$ versus $V-I$ colors, we have found that the BC03 models provide a good overall match to the observed colors of ∼100,000 clusters from the PHANGS-HST survey (J. A. Turner et al. 2021; D. Maschmann et al. 2024; K. F. Henny et al. 2025; D. Thilker et al. 2025). Independent age estimates from spectroscopy and H_α bubble size also give results similar to the predictions from the BC03 models (B. C. Whitmore et al. 2011, 2020; R. Chandar et al. 2016).

2.3.2. Refined Age Estimates from H_α Superbubble Sizes

B. C. Whitmore et al. (2011) demonstrated that the radii of H_α superbubbles around young clusters in M83 tend to increase with ages estimated from SED fitting. H_α emission is observed essentially on top of the broadband stellar-continuum emission for the youngest clusters, is in a small bubble for slightly older clusters, and has formed a fairly large bubble or shell (typically 20–80 pc) by an age of 3–5 Myr. K. Hollyhead et al. (2015) performed a similar analysis in M83 and concluded that the clusters have removed their natal gas in <4 Myr, in good agreement with the B. C. Whitmore et al. (2011) timescale. Other studies with similar results include S. Hannon et al. (2022), E. J. Watkins et al. (2023), A. Pedrini et al. (2024), and M. Rodríguez et al. (2025).

Using these results, we divide clusters with integrated colors that fall in the 1–4 Myr box into 1, 2, 3, and 4 Myr adopted age bins based on their estimated H_α superbubble size. Given 20 clusters, we assign them into four groups of five each, as described below. To facilitate this relative ordering by age, we make simple visual estimates of the size of the superbubble, by measuring the distance in pixels from the cluster to the nearest H_α feature that appears to be part of the shell. The results are included in Table 1, and are used to separate the sample into the appropriate age bins for the clusters in the 1–4 Myr box, also included in Table 1. We note that most of the superbubbles are quite erratic in shape, making more complete measurement (e.g., with minimum and maximum shell radii, as used in K. Hollyhead et al. 2015 for typically better defined bubbles) unwarranted.

It is important to note that the adopted estimates in the 1–4 Myr age range should be considered as both tentative and relative (rather than absolute), since there are many physical processes operating during the early life of a H II region that may modify the simple linear approximation used to assign age estimates for these very young clusters. Examples are inclusion of nebular emission in the models (D. Thilker et al. 2025), variations in escape fraction (e.g., A. T. Barnes et al. 2022; J. W. Teh et al. 2023), coupling efficiency of stellar feedback (e.g., R. Weaver et al. 1977; M. S. Oey & G. García-Segura 2004; O. V. Egorov et al. 2023), modification of expansion velocities as a function of time (E. J. Watkins et al. 2023), age spread in the formation of low- versus high-mass stars (e.g., G. Brown & O. Y. Gnedin 2022), and different pressure of the ISM as a function of environment (e.g., as shown by a correlation of the sizes of H II regions with distance from the center of the galaxy; A. Pedrini et al. 2024). However, with a range of only 1–4 Myr for clusters in this part of the color–color diagram, essentially any reasonable scenario is going to give maximum errors of 1 or 2 Myr for a particular cluster. We take a closer look at the clusters in the 1–4 Myr box in Appendix A. One of the results is the demonstration that there is a roughly even distribution of clusters from very compact to large bubbles, consistent with our assumption of an even distribution of ages from 1 to 4 Myr.

We note that nebular emission has not been included in the BC03 models shown in Figure 3. This will spread the predicted colors out slightly for 1, 2, 3 Myr ages, but the 1–4 Myr box is large enough that this will not affect the overall results very much (see D. Thilker et al. 2025, for a discussion).

A sanity check is possible by examining the results from E. J. Watkins et al. (2023), who identified 34 superbubbles in NGC 628, two of which are shown in Figure 4. The bottom bubble (i.e., denoted Watkins—bubble #1) is #4 in the list of 12 "perfect" bubbles in NGC 628 in Table 2 of E. J. Watkins et al. (2023), with a CO expansion velocity of 10 km s^{-1} and an estimated age of 3 Myr. The top bubble (i.e., denoted Watkins—bubble #2) is smaller and less resolved, and hence is not in the final catalog of 12 objects. However, Watkins' estimate for this object (E. J. Watkins, private communication) is 1–2 Myr. These age estimates are quite compatible with our use of bubbles to estimate cluster ages between 1 and 4 Myr. In particular, we note that the "central" cluster in the bottom superbubble is cluster 6276, which is in our training sample with an adopted age of 4 Myr. Furthermore, the morphology of the top bubble is similar to the 2 and 3 Myr bubbles in Figure 5.

We also note that our estimated ages are consistent with those for young star clusters and H II regions in the Milky Way (e.g., E. Churchwell et al. 2006) and Magellanic Clouds. For example, G. De Marchi et al. (2011), P. A. Crowther & N. Castro (2024), and K. Fahrion & G. De Marchi (2024) find ages in the range 2–4 Myr for various components of the central region of 30 Dor (i.e., R136 and NGC 2070).

Figure 4 also demonstrates that the outflow that created the superbubbles has removed most of the gas and dust from within the effective photometric apertures used for our study (shown in the middle left panel as the red solid line for HST and NIRCAM data, the orange dashed line for the F770W data, and the yellow dotted line for the F2100W data) in just a few Myr. It is primarily the rapid removal from the aperture of the gas and dust, and the corresponding nebular, PAH, and IR dust emission, that reduces the near- and mid-infrared flux and produces the signal that allows us to differentiate the youngest star clusters.

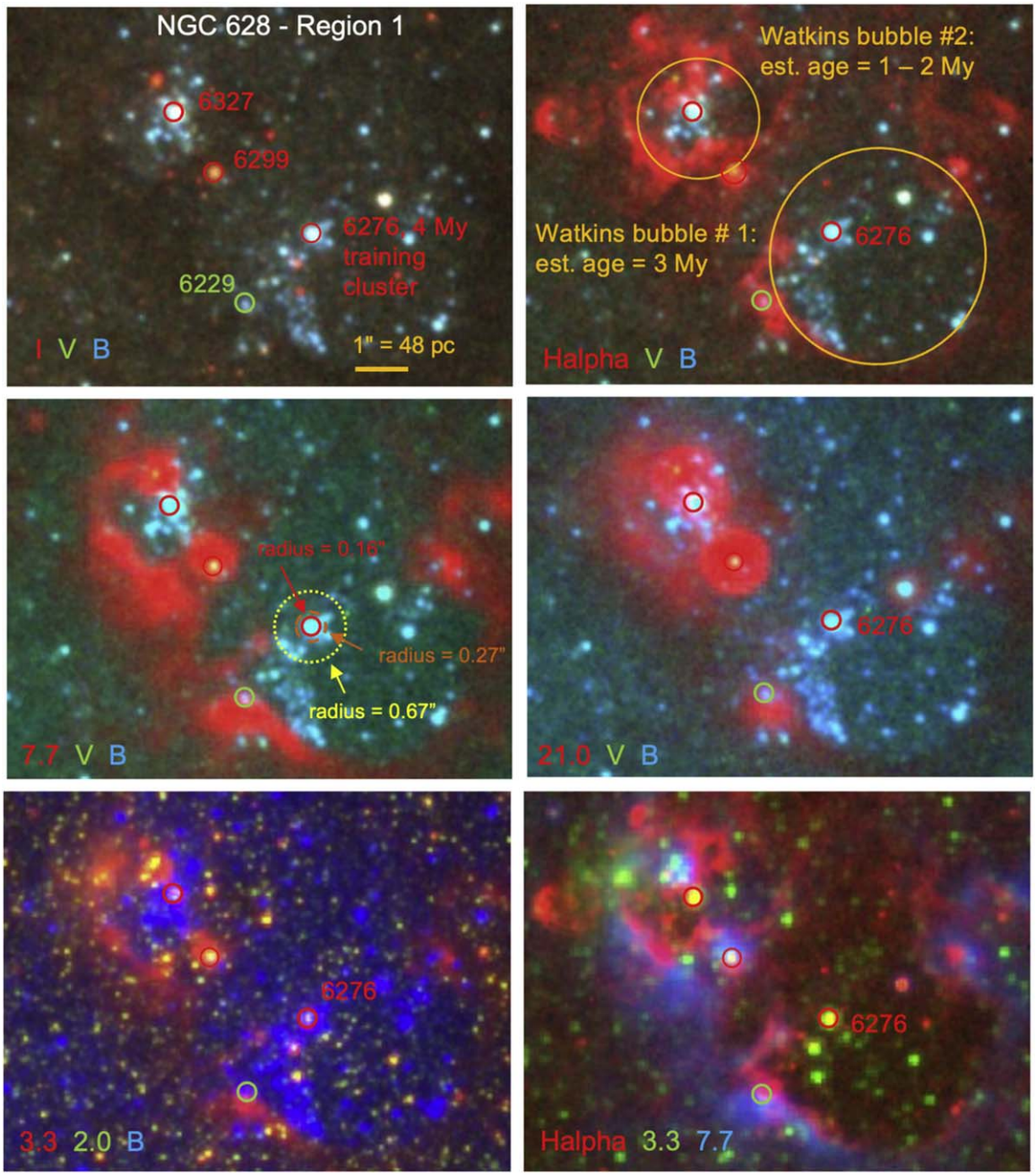

Figure 4. Images using several color combinations are shown of Region 1 in NGC 628 (from B. C. Whitmore et al. 2025, in preparation), which contains two superbubbles from E. J. Watkins et al. (2023) (i.e., the yellow circles in the upper right panel), where age estimates have been made based on the observed expansion velocities in CO. There are four clusters from the human-classified compact cluster catalog (D. Maschmann et al. 2024) (Class 1 in red and Class 2 in green), one of which (6276) is one of the 4 Myr training clusters used in the current paper. The sizes of the apertures used in the optical (red), 7.7 (orange), and 21.0 (yellow) μm observations are shown in the middle left panel.

2.4. Selection of Clusters for SED Templates

With our two associated age-dating methods in hand, we select the five most massive clusters (based on the D. Thilker et al. 2025) estimates at each adopted age to create empirical SED templates. Figures 5 and 6 show snapshots of all 40 clusters used for these templates. A careful examination of these images reveals several things.

1. For the clusters with adopted ages of 1 Myr clusters, Hα is right on top of the central cluster (always just above the small red cross).
2. The H_α superbubble becomes less well defined from 3 Myr through 4 Myr, and H_α emission is generally gone by 5 Myr. For older sources, we do not generally see H_α clearly associated with the cluster in all but cluster 2352 (discussed further below as an outlier), just occasionally what appears to be unassociated diffuse H_α emission based on the morphology (i.e., not ring-like and not roughly centered on the cluster).
3. Hα and 3.3 μm PAH emission have somewhat similar morphologies, although in many of the cases (e.g., sources 1767, 4505, 5418, 7280, 3538, 6681, 1905, 1343, 2972, and 5434), the central cluster appears fainter in

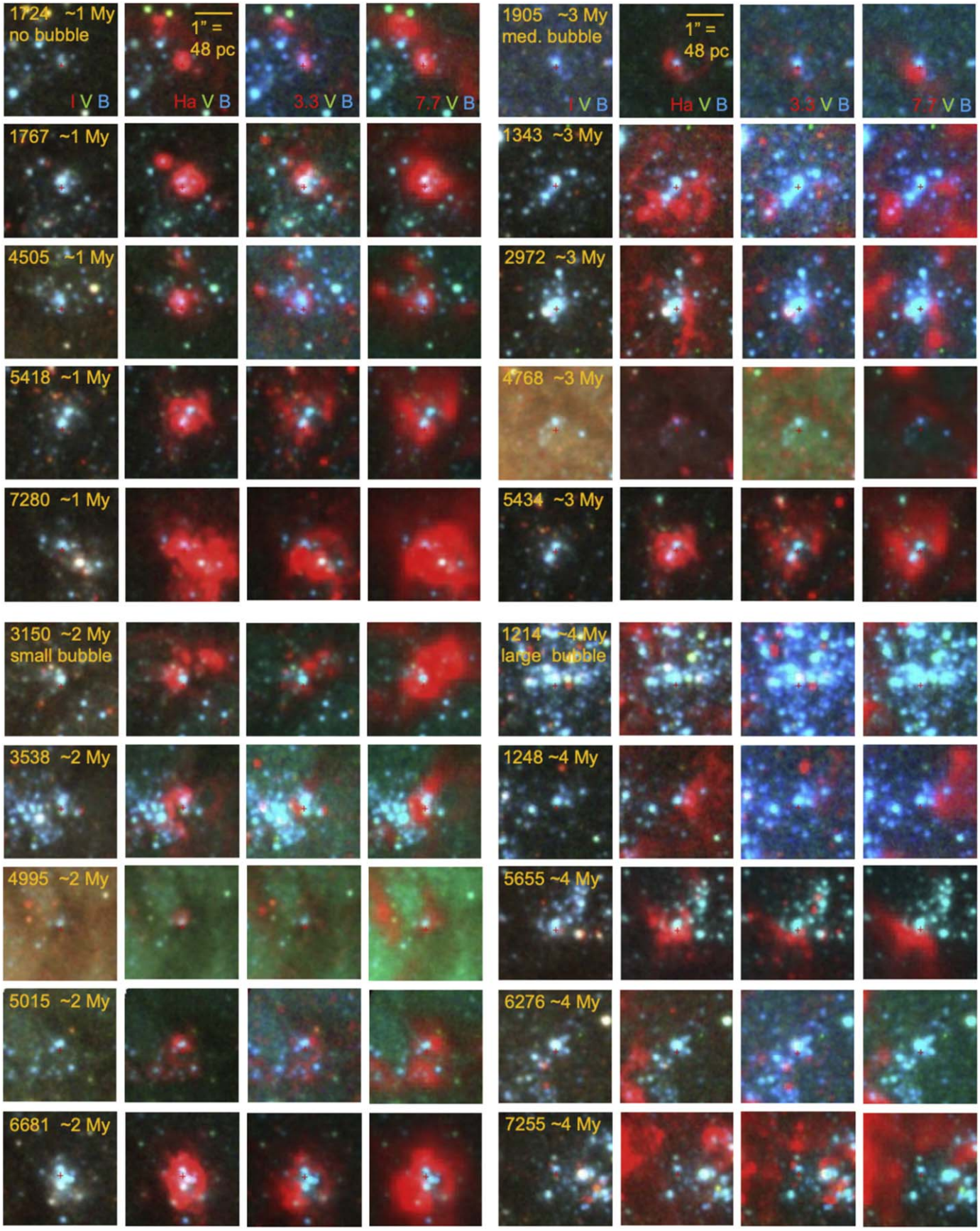

Figure 5. Snapshots of the 1–4 Myr training set clusters. The cluster ID is shown in yellow, along with the adopted age (see text). The color combinations used for the snapshots, and a size scale, are shown in the top row. The program cluster is just above the small red cross in all cases.

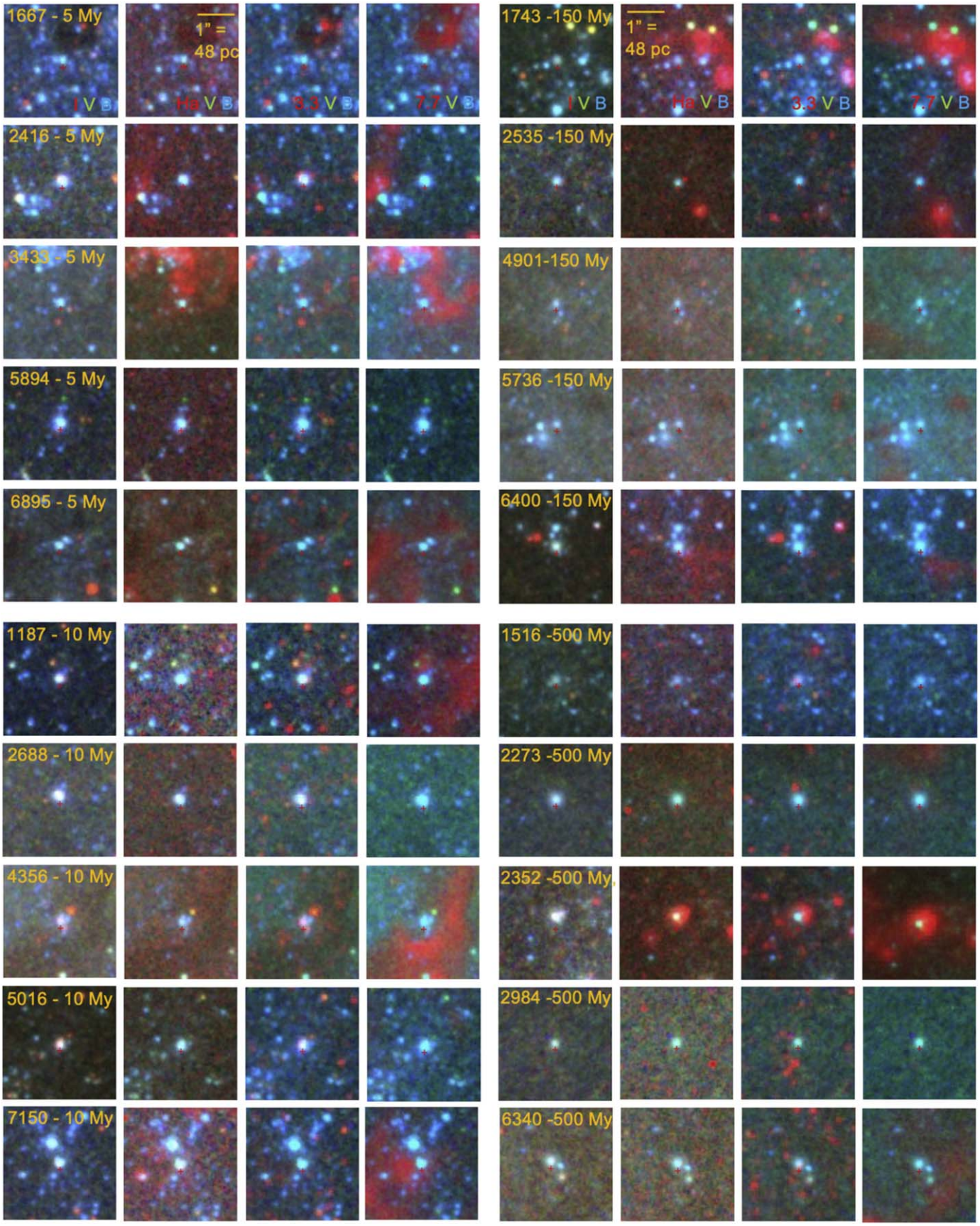

Figure 6. Same as Figure 5 for 5–500 Myr training set clusters.

3.3 μm, and the superbubble appears slightly larger and/or the ring less-well defined than the H_α emission. This may be due to the preferential destruction of smaller PAH dust grains associated with 3.3 μm emission (e.g., S. C. Madden et al. 2006; M. S. Povich et al. 2007; A. Maragkoudakis et al. 2018; O. V. Egorov et al. 2023). We return to this point in Section 3.3.

4. The 7.7 and 21 μm (not shown) maps have morphologies similar to those of the H_α maps, albeit with lower resolution. The resemblance between the 7.7 and 3.3 μm morphologies is not as good, again perhaps because of earlier destruction of the 3.3 μm dust grains.

We note that, in one case, two clusters (5418 and 5434) are part of a close pair, with a separation of about 10 pixels. As in previous studies (e.g., B. C. Whitmore et al. 2021) we use a separation of five WFC3 pixels as a criteria to reduce the redundancy and double counting. This is the only pair with a separation of less than 20 pixels in the sample, hence it has only a minimal effect on the results.

The key takeaway from our investigation of the 40 clusters in NGC 628 that will be used to create SED templates is that by the time clusters are ≈5 Myr old, little to no associated H_α, PAH, or IR dust continuum emission remains. The absence of strong gas and dust tracers in the 5 and 10 Myr samples, and the agreement of the observed IR SEDs with the TODDLERS predictions (discussed in Section 4.1), provide further support for the conclusion that there is little or no strong PAH or IR dust emission locally associated with clusters older than about 5 Myr.

2.5. Outlier Rejection

It is often the case that there are important lessons to be learned from outliers. The small sample used in this pilot work allows us to study each cluster in detail and identify objects to reject from the sample in order to reduce the scatter and improve the reliability.

A careful look at Figures 5 and 6 reveals three important issues that have been used to remove three of the clusters from our sample, as listed in Table 1. The first is related to the high background, and likely environmental dependencies of galaxies in the inner region of NGC 628. Cluster 4768 (3 Myr sample) is the primary example, showing a high background in all colors, as well as a potential environmental dependence caused by the inner H II regions being systematically smaller than H II regions in the outer part of the galaxy (e.g., see Figure 1), probably because of the higher gas pressure in the inner region (e.g., O. V. Egorov et al. 2023; A. Pedrini et al. 2024). This cluster would have negative fluxes in the F1000W and F1130W filters if left in the sample. A similar cluster found in the inner region is 4995 (2 Myr sample). This second object in the inner galaxy has not been eliminated from the sample, since the resulting photometry is not as discrepant when compared with the other clusters with age estimates of 2 Myr.

The second issue is relevant for cluster 7255 (4 Myr sample). This cluster has strong emission features in the outskirts that fall into the sky annulus (see Figure 5), resulting in the oversubtraction of all the emission features. This cluster would have negative fluxes in the F335M and all four of the MIRI filters if left in the sample.

The third issue is relevant for cluster 2352 (500 Myr sample). This is clearly a very young cluster, as evidenced by the strong emission in H_α, F335M, and F770W. It is probably in the "wrong" part of the color–color diagram due to stochasticity (i.e., the presence of one or more red supergiants along with several blue stars). A careful look shows the presence of at least five point-like objects; hence, it is likely a compact association rather than a cluster. This cluster would have large positive flux measurements in all MIRI bands, with values appropriate for a 2 or 3 Myr cluster, if left in the sample.

This is an important reminder that errors and noise from a variety of sources (e.g., classification errors, stochasticity, crowding, photometric errors, etc.) are present and may obscure the fundamental correlations if care (e.g., manual examination) is not taken into account when selecting a training cluster sample.

3. Results: New Cluster SED Templates

3.1. Creation of Empirical Cluster SEDs

We now use our measured photometry for the five most massive (generally brightest) clusters in each of the degeneracy-free boxes, coupled with information on the size and morphology of the H II region superbubbles, to create new empirical templates for 1, 2, 3, 4, 5, 10, 150, and 500 Myr star clusters—and by extrapolation, for all cluster ages, because we will show that the observations for all clusters older than 10 Myr are compatible with BC03 stellar-continuum models. Hence, our templates for clusters older than 10 Myr are simply taken from the BC03 models.

We start by plotting the mean flux of the five clusters at each adopted age measured in each filter. These values are listed in Table 2, along with the corresponding prediction from the BC03 solar-metallicity, stellar-continuum models in parentheses for comparison. The three outliers discussed in the last section are not included. The mean fluxes for each adopted age are plotted in the top left panel of Figure 7, where they have been normalized to 1 in the F814W (*I*) band. The fluxes are corrected for a small amount of reddening for each cluster (see Table 1), based on the original HST fits from J. A. Turner et al. (2021). The lower panels show the measured fluxes for all five (four in the three cases where an outlier has been removed) clusters in each age bin to give a sense of the scatter.

A great deal of insight can be obtained by carefully examining Figure 7. Here, we note some important features from the mean flux distributions that will be important for building our empirical templates.

In the optical bands using Hubble data (i.e., the six leftmost data points from the F275W, F336W, F435W, F555W, F658N = Hα, and F814W filters), the mean values agree with the BC03 stellar-continuum models (i.e., the dashed lines; see also the numbers in parenthesis in Table 2) remarkably well in almost all cases, providing strong support for both the age estimates of our training sets and the use of the BC03 models. Only the 1, 2, and 3 Myr clusters show any Hα emission that sticks out above the stellar continuum.

Note that all of the data points in the optical part of the SED are well above the detection limits shown by the black triangles, hence these are high signal-to-noise observations. The detection limits are determined using the mean of the three lowest values of the standard deviations determined using the five clusters (or in some cases, four) in each of the six age bins separately. Only the three lowest standard deviations are used

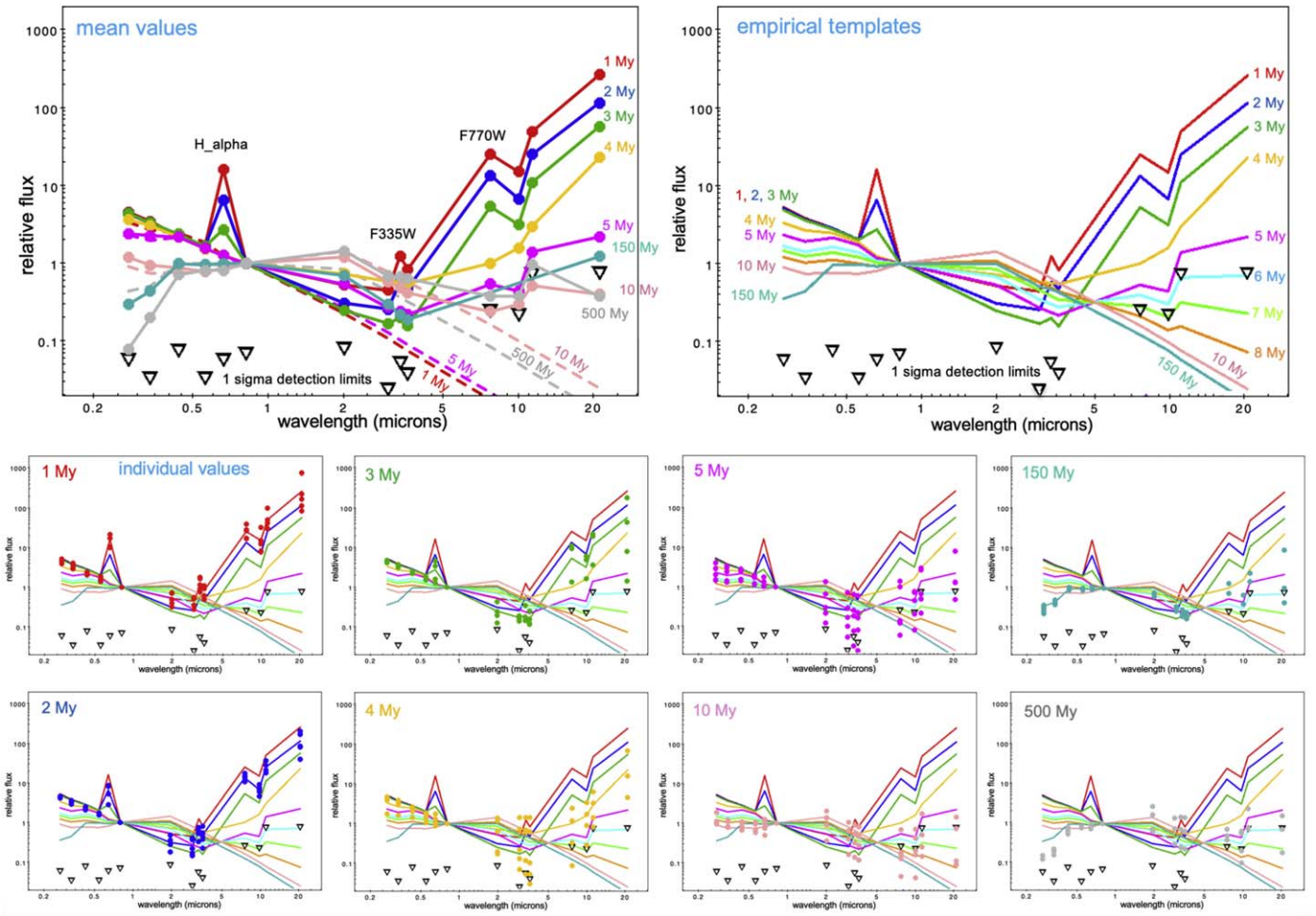

Figure 7. Figure showing how the mean-value versions of the empirical templates (upper right panel) are derived from the observations of the training set (upper left panel). The dashed lines are from the BC03 stellar-continuum models. The black triangles are the 1σ detection limits. The individual clusters are shown in the bottom panel for the five clusters in each sample, although in some cases there are fewer data points because a cluster is an outlier (see Section 2.5) or is off the bottom of the diagram.

to avoid bins with very large standard deviations (generally the 4, 5, and 10 Myr bins).

In the near-IR bands using NIRCAM on JWST (i.e., F200W, F300M, F335M, and F360M—the central four data points) the fluxes of the 1 and 2 Myr clusters are quite strong. For the 3 Myr sample, we find that the mean values drop significantly and are essentially those expected from stellar-continuum emission alone (i.e., the dashed lines). This is likely because the small dust grains responsible for emission in this wavelength range have very quickly been removed by outflows or destroyed by UV radiation (e.g., K. M. Sandstrom et al. 2012; O. V. Egorov et al. 2023; J. Sutter et al. 2024). For ages of 5 Myr and older, red supergiants start appearing and the near-IR flux recovers and is much higher, reaching a peak at about 10 Myr where the flux in the NIRCAM filters is as strong as the brightest PAH emission in F335M for 1 Myr clusters! In particular, note the generally good agreement between the predicted BC03 stellar continuum and the data points for 10, 150, and 500 Myr clusters. *This is an important point*: the only time that the NIRCAM flux is dominated by PAH or IR dust emission is for the 1 and 2 Myr clusters; in older clusters, the near-IR flux is primarily from the stellar continuum.

The scatter between the points in the near-IR bands is quite small for ages 1, 2, and 3 Myr, but is much larger for ages 4 and 5 Myr. This probably reflects the irregular and patchy morphology of the older bubbles, as shown in Figures 5 and 6. While many of the data points for the 4 and 5 Myr cluster are consistent with the stellar-continuum values for ages of around 5 Myr (as shown by the dashed lines in the upper left panel), other points are higher and are more consistent with the predictions for ages of 7–10 Myr. It is not clear whether this is due to more uncertain age estimates in this age range based on the BC03 models (see K. F. Henny et al. 2025), larger differences in morphology for the clusters with ages around 4 Myr, or larger photometric uncertainties since many of these clusters are near the 1σ detection limits.

We have developed two versions of the empirical 4–8 Myr cluster SED models to reflect their larger scatter in the near-IR: one using the mean values for 4–8 Myr clusters (version 1) and one using the stellar-continuum models in this age range (version 2). For simplicity, only the mean models are shown in the SED empirical templates shown in Figure 7; both versions of the templates are shown in Section 3.4, where we discuss the IR color–color diagrams. Table 3 includes both versions of the empirical templates, with the mean-value version shown in bold and the stellar-continuum version in bold and italic.

For the mid-IR bands using MIRI on JWST (i.e., the rightmost four points), we find a rapid increase in flux as a

Table 2
Mean Relative Flux Values of the Eight Age Bins and Comparison to BC03 Using Small-aperture Photometry[a]

Wave[b]	1 Myr	2 Myr	3 Myr	4 Myr	5 Myr	10 Myr	150 Myr	500 Myr
0.275	4.56 (5.265)	4.34 (5.187)	4.40 (4.881)	3.67 (3.385)	2.40 (2.324)	1.20 (0.915)	0.30 (0.357)	0.08 (0.095)
0.336	3.49 (3.827)	3.32 (3.786)	3.34 (3.620)	3.06 (2.687)	2.29 (1.966)	0.95 (0.746)	0.44 (0.441)	0.20 (0.189)
0.435	2.24 (2.819)	2.35 (2.810)	2.38 (2.765)	2.20 (2.455)	2.18 (2.178)	0.88 (0.771)	0.99 (0.983)	0.71 (0.732)
0.555	1.66 (2.056)	1.65 (2.059)	1.65 (2.041)	1.54 (1.881)	1.57 (1.728)	0.79 (0.748)	0.96 (0.983)	0.82 (0.848)
0.658	**16.20**[c] (1.314)	**6.61** (1.317)	**2.74** (1.312)	1.29 (1.260)	1.26 (1.204)	0.86 (0.807)	1.01 (0.918)	0.82 (0.859)
0.814	1.0	1.0	1.0	1.0	1.0	1.0	1.0	1.0
2.0	**0.53** (0.211)	**0.31** (0.207)	**0.25** (0.205)	**0.73** (0.228)	**0.54** (0.268)	1.21 (1.430)	0.70 (1.006)	1.46 (1.072)
3.0	**0.45** (0.101)	**0.26** (0.099)	**0.17** (0.098)	**0.59** (0.109)	**0.27** (0.130)	0.58 (0.781)	0.30 (0.510)	0.69 (0.566)
3.35	**1.25** (0.080)	**0.59** (0.078)	**0.20** (0.078)	**0.57** (0.087)	**0.24** (0.104)	0.48 (0.650)	0.22 (0.473)	0.67 (0.508)
3.6	**0.84** (0.069)	**0.48** (0.068)	**0.16** (0.067)	**0.55** (0.075)	**0.22** (0.090)	0.42 (0.575)	0.19 (0.433)	0.64 (0.475)
7.7	**25.4** (0.016)	**13.60** (0.016)	**5.36** (0.016)	**1.01** (0.018)	**0.54** (0.022)	0.24 (0.164)	−0.02 (0.123)	0.38 (0.134)
10.0	**15.0** (0.009)	**6.77** (0.009)	**3.15** (0.009)	**1.59** (0.010)	**0.44** (0.013)	0.30 (0.101)	−0.05 (0.078)	0.38 (0.092)
11.3	**49.4** (0.007)	**25.10** (0.007)	**11.00** (0.007)	**2.99** (0.008)	**1.41** (0.010)	0.52 (0.079)	−0.64 (0.597)	0.98 (0.067)
21.0	**266.0** (0.002)	**116.5** (0.002)	**57.6** (0.002)	**23.0** (0.002)	**2.20** (0.003)	0.40 (0.025)	1.23 (0.017)	0.38 (0.013)

Notes.
[a] The values without parentheses are the mean values (using small-aperture photometry) for the clusters in the training set for the eight age bins used as a skeleton to derive the SED templates at all ages (see Figure 7). The values in parentheses are the corresponding values from the solar-metallicity, stellar-continuum BC03 models for comparison. The values are ratios using Janskys, normalized to the F814W filter. Note that H_α and PAH (i.e., 3.3, 7.7, and 11.3 μm) values in this table have not been continuum subtracted, but they have been continuum subtracted in Figure 11. The mean values have been corrected for reddening using the Milky Way extinction coefficients and the $E(B-V)$ values in Table 1.
[b] Approximate wavelength in μm.
[c] The bold numbers are the only ones that have been changed in the final empirical templates in Table 3 (mean-value version), based on observed enhancements over the BC03 models in H_α, PAH, and IR dust continuum emission in our training set.

Table 3
Empirical Templates[a] Using Small-aperture Photometry

Wave[b]	1 Myr	2 Myr	3 Myr	4 Myr	5 Myr	6 Myr	7 Myr	8 Myr	9 Myr	10 Myr	100 Myr	500 Myr	1 Gyr[c]
0.275	5.265	5.187	4.881	3.385	2.324	1.688	1.464	1.214	0.941	0.915	0.441	0.095	0.034
0.336	3.827	3.786	3.620	2.687	1.966	1.444	1.252	1.027	0.772	0.746	0.511	0.189	0.113
0.435	2.819	2.810	2.765	2.455	2.178	1.645	1.417	1.134	0.791	0.771	1.010	0.732	0.438
0.555	2.056	2.059	2.041	1.881	1.728	1.399	1.233	1.013	0.761	0.748	0.998	0.848	0.661
0.658	**16.2**	**6.61**	**2.74**	1.260	1.204	1.101	1.030	0.927	0.819	0.807	0.934	0.859	0.824
0.814	1.0	1.0	1.0	1.0	1.0	1.0	1.0	1.0	1.0	1.0	1.0	1.0	1.0
2.0	**0.53**	**0.31**	**0.25**	**0.73**, *0.23*[d]	**0.54**, *0.27*	**0.68**, *0.467*	**0.87**, *0.691*	**1.10**, *1.045*	1.394	1.430	0.845	1.072	1.243
3.0	**0.45**	**0.26**	**0.17**	**0.59**, *0.11*	**0.27**, *0.13*	**0.35**, *0.240*	**0.45**, *0.366*	**0.59**, *0.564*	0.759	0.781	0.446	0.566	0.654
3.35	**1.25**	**0.59**	**0.20**	**0.57**, *0.09*	**0.24**, *0.10*	**0.30**, *0.196*	**0.39**, *0.301*	**0.50**, *0.468*	0.632	0.650	0.367	0.508	0.584
3.6	**0.84**	**0.48**	**0.16**	**0.55**, *0.07*	**0.22**, *0.09*	**0.28**, *0.171*	**0.35**, *0.264*	**0.44**, *0.413*	0.559	0.575	0.322	0.475	0.551
7.7	**25.4**	**13.60**	**5.36**	**1.01**	**0.54**	**0.40**	**0.29**	**0.21**	0.157	0.164	0.085	0.134	0.155
10.0	**15.0**	**6.77**	**3.15**	**1.59**	**0.44**	**0.30**	**0.21**	**0.14**	0.096	0.101	0.051	0.092	0.108
11.3	**49.4**	**25.10**	**11.0**	**2.99**	**1.41**	**0.68**	**0.32**	**0.16**	0.075	0.079	0.040	0.067	0.077
21.0	**266.0**	**116.5**	**57.6**	**23.0**	**2.20**	**0.71**	**0.23**	**0.07**	0.024	0.025	0.012	0.013	0.015

Notes. These empirical templates (using small-aperture photometry) are based on a combination of the "skeleton" templates based on the observations of the training set (Table 2), and the solar-metallicity, zero-reddening, stellar-continuum BC03 models (black and italic numbers), as discussed in Section 3, The bold numbers are the only ones that have been changed, based on observed enhancements in H_α, PAH, and IR dust continuum emission in our training set. The full template for all individual ages (i.e., filling in the BC03 stellar-continuum values for older ages) is available at https://archive.stsci.edu/hlsp/phangs/phangs-cat
[a] The values in this table are ratios using Janskys, normalized to the F814W filter. Note that H_α and PAH (i.e., 3.3, 7.7, and 11.3 μm) values in this table have not been continuum subtracted, but they have been continuum subtracted in Figure 11. The values have been corrected for reddening using the Milky Way extinction coefficients and the $E(B-V)$ values in Table 1 for the training set.
[b] Approximate wavelength in μm.
[c] After 1 Gyr, lower-metallicity BC03 models should generally be used. See B. C. Whitmore et al. (2023a) and D. Thilker et al. 2025, who use 1/50 solar-metalicity values, appropriate for old globular clusters.
[d] When two values are listed, the bold values are for version 1 (mean-value template) while italic values are for version 2 (lower-limit template). See Section 3 for discussion.

function of wavelength for the 1 and 2 Myr clusters, with the 1 Myr flux measurements being slightly higher at all wavelengths. The scatter in the fluxes between the five clusters at each age is quite small (≈50%), so the shapes of these templates are quite secure—and are, in fact, quite similar. The 5 Myr data points are much lower, and only slightly above the detection limit in the MIRI bands. For older ages (i.e., 10, 150, and 500 Myr), the MIRI flux values are below the detection limit in most cases (i.e., several of the points are negative and do not show up in the plots showing the five clusters in each age range in the bottom of Figure 7).

Based on the mean values shown in the upper left panel of Figure 7, and the various points outlined below, we create template SEDs as shown in the upper right panel of Figure 7. This series of different age templates provide a preliminary but important benchmark/comparison set that can be used to estimate cluster ages and improve model predictions using a combination of HST and JWST data. Here are the primary steps used to build the templates.

1. For the optical/HST bands, we use the solar-metallicity BC03 stellar-continuum models for all ages and filters, except for the F658N (H_α) filter for ages 1, 2, and 3 Myr, where we use the mean observed values.
2. For the NIR/NIRCAM bands, we have two models, version 1 (mean-value template) using the mean values for ages 1 through 8 Myr, and version 2 (lower-limit template) using mean values for ages 1–3 Myr but BC03 stellar-continuum values for ages 4–8 Myr. For all other ages, we use the BC03 stellar-continuum values.
3. For the MIR/MIRI bands, we use the mean values for the 1, 2, 3, 4, and 5 Myr templates. For the 6, 7, and 8 Myr templates, because the 5 Myr data are barely above the brightness limits, we interpolate between the 5 Myr mean measured flux and the predicted BC03 stellar continuum for 9 Myr, in lieu of reliable measurements in this age range. While this is somewhat ad hoc, it results in a relatively smooth evolution in the template SEDs from 1 to 9 Myr, and it agrees with the stellar-continuum position of the 10 Myr clusters in the IR-optical color–color diagram, as we discuss in Section 3.4.

Table 3 provides the values for the two versions of the templates established in this paper. For both versions, most values are taken from the BC03 solar-metallicity stellar-continuum, $A_V = 0.0$ models. In version 1 (mean-value template = bold values), the mean values from the training set are used in all cases. For version 2, (lower-limit template = italic values) the mean (bold) values are used for most of the values, but they are superseded by the Italic values when appropriate (i.e., BC03 values are used for NIRCAM for ages 4–8 Myr).

Our full templates include predictions for all 14 HST+JWST filters presented here at all 109 ages (i.e., ranging from 1 Myr to 13.75 Gyr) included in the CIGALE implementation of the G. Bruzual & S. Charlot (2003) models. This is done by filling in all values that are not bold or italic in Table 3 with the stellar-continuum values. The full templates are available online.[32]

[32] https://archive.stsci.edu/hlsp/phangs/phangs-cat

In principle, we could attempt to construct SED templates using PHANGS clusters of all ages. This approach is complicated by the age/reddening/metallicity degeneracy, which makes age estimates less certain outside of the degeneracy-free boxes we have used in this paper. Our approach to evaluate the SEDs using regions in the color–color diagram where we most trust the ages allows us to (1) determine new empirical templates for the very youngest ages where the BC03 models do not fit the observed SEDs in the IR and (2) to establish that, for 10, 150, and 500 Myr, the BC03 models agree with the observations relatively well. We therefore use the BC03 models for clusters of all ages greater than 10 Myr.

As appropriate for a pilot study, these SED templates should be considered preliminary. We expect it will be possible to build more accurate templates in the near future, because of both the coming availability of H_α observations for all 19 galaxies that have JWST observation (R. Chandar et al. 2025) and the inclusion of more clusters from more galaxies in our training set.

3.2. Nearly Embedded Cluster Candidate SEDs

With the optically selected cluster templates in hand, we now check if nearly embedded clusters have similar SEDs in the infrared, so they can be age-dated using the same empirical templates.

Samples of nearly embedded cluster candidates were obtained from two studies: H. Hassani et al. (2023) (using photometry convolved to match the $0\farcs67$ effective radius of the F2100W filter) and M. Rodríguez et al. (2025), using the small-aperture photometry described in Section 2.4 and used for our training set, empirical templates, and throughout the rest of the paper.

For the purposes of the current paper, the selection criteria designed to identify roughly a dozen of the best nearly embedded cluster candidates from the H. Hassani et al. (2023) sample was to have: (1) $2 <$ F335M − F300M < 3 (i.e., very strong F335W PAH emission) where the normalized flux values from Table 4 are used for the evaluation, (2) F200W flux > 0.006 mJy (i.e., strong continuum sources), and (3) normalized F814W between 0.0 and 0.13 (i.e., "nearly embedded" in the optical).

A similar set of selection criteria for nearly embedded cluster candidates from the M. Rodríguez et al. (2025) sample was used to select the 12 of 53 objects from the 5σ sample of 3.3 μm-emitters that have the following attributes: (1) F335M − F300M > 0.9 (where the normalized flux values from Table 5 are used for the evaluation), (2) F200W flux > 0.0015 mJy, and (3) normalized F814W between 0.0 and 0.4. See M. Rodríguez et al. (2025) for details on how the original sample of 5σ, 3.3 μm emitters were selected. We note that the original selection of objects identified in the full Hassani catalog used the F2100W filter. The secondary selection using the F335M − F300M criteria was designed to better match the criteria used in the M. Rodríguez et al. (2025) catalog so that a fairer comparison could be made.

Figures 8 and 9 show snapshots of the 12 (H. Hassani et al. 2023) nearly embedded cluster candidates using several combinations of the filters to make the image, starting with the optical IVB image on the left. Four of these clusters are coincident with or near the M. Rodríguez et al. (2025) sample of nearly embedded cluster candidates, as shown by the yellow

Table 4
Normalized Flux Values for Nearly Embedded Cluster Candidates from H. Hassani et al. (2023)[a] Using Convolved Large-aperture Photometry

ID	R.A.	Decl.	0.435	0.555	0.814	2.0	3.0	3.3	3.6	7.7	10.0	11.3	21.0	2.0 flux[b]
H 319	24.193756	15.758428	0.03	0.05	0.07	1.0	1.18	3.78	3.07	42.23	18.46	51.06	164.83	0.0237
H 338	24.177973	15.760403	0.01	0.01	0.04	1.0	0.99	3.55	2.25	46.48	16.88	53.06	112.53	0.0067
H 368	24.196670	15.763851	0.07	0.09	0.13	1.0	0.9	3.08	2.0	37.64	13.59	43.12	85.43	0.0256
H 442	24.196642	15.769243	0.06	0.07	0.12	1.0	0.91	3.25	2.21	45.12	21.46	57.13	191.79	0.0209
H 447	24.196194	15.769644	0.0	0.01	0.03	1.0	0.91	3.07	2.02	42.03	16.6	49.59	171.53	0.0193
H 516	24.182970	15.773744	0.09	0.1	0.13	1.0	1.06	4.0	2.53	49.15	22.16	64.31	192.34	0.0091
H 538	24.185340	15.775685	0.07	0.09	0.1	1.0	1.0	3.45	2.28	48.04	14.85	51.05	119.11	0.0165
H 572	24.164656	15.777629	0.08	0.09	0.11	1.0	0.85	3.03	1.97	36.92	13.09	42.62	96.36	0.0069
H 932	24.149864	15.796673	0.03	0.04	0.06	1.0	0.99	4.0	2.5	49.95	19.38	57.56	131.78	0.0116
H 986	24.179390	15.800398	0.02	0.03	0.06	1.0	0.87	2.89	1.91	32.51	13.5	38.51	107.91	0.0159
H 1000	24.179485	15.800799	0.04	0.05	0.06	1.0	1.03	3.38	2.1	39.51	14.22	44.93	92.26	0.0067
H 1067	24.179934	15.805174	0.01	0.02	0.06	1.0	0.93	3.2	2.33	40.81	13.1	42.44	90.14	0.0102

Notes.
[a] Selected nearly embedded cluster candidates from H. Hassani et al. (2023), as shown in Figures 8 and 9. See Section 3.2 for selection criteria. The flux values in this table are ratios using Janskys, normalized to the F200W filter. The values have not been corrected for extinction, since we do not have $E(B-V)$ values from an SED fit using the HST data in most cases.
[b] The 2.0 flux in mJanskys can be used to convert the relative flux values in this table to absolute values.

Table 5
Normalized Flux Values of Nearly Embedded Cluster Candidates from M. Rodríguez et al. (2025)[a] Using Small-aperture Photometry

ID	R.A.	Decl.	0.435	0.555	0.658	0.814	2.0	3.0	3.3	3.6	7.7	10.0	11.3	21.0	2.0 flux[a]
R 11139	24.177998	15.760442	0.11	0.12	0.0	0.4	1.0	0.79	2.94	1.84	31.81	14.95	55.42	212.06	0.00364
R 15153	24.196577	15.763497	0.47	0.47	12.52	0.27	1.0	1.56	3.03	2.98	19.19	5.57	25.81	165.2	0.00185
R 25163	24.196716	15.76925	0.02	0.07	3.14	0.37	1.0	0.69	1.91	1.34	38.92	31.03	108.86	790.02	0.00459
R 26027	24.19616	15.769671	−0.01	−0.01	1.25	0.07	1.0	0.82	2.87	1.92	40.87	20.08	69.04	371.0	0.00893
R 37861	24.16679	15.775292	0.2	0.0	0.0	0.21	1.0	0.87	2.26	1.81	31.71	14.18	57.59	197.7	0.00484
R 41648	24.170889	15.776963	0.04	0.05	0.0	0.13	1.0	0.71	2.04	1.4	27.78	12.06	44.9	176.78	0.00521
R 43865	24.185879	15.777877	−0.34	0.05	0.0	0.32	1.0	1.54	4.18	2.79	56.2	26.06	113.77	680.95	0.00229
R 60799	24.170343	15.783778	0.17	0.11	0.0	0.28	1.0	0.79	3.03	2.04	42.21	18.47	74.15	331.07	0.00672
R 62243	24.170837	15.784217	0.95	0.83	0.0	0.4	1.0	0.71	1.63	1.23	20.5	7.75	31.43	82.93	0.00425
R 100286	24.184801	15.800811	0.01	0.01	0.0	0.2	1.0	0.77	2.57	1.69	34.11	21.58	67.5	247.47	0.00584
R 119112	24.196215	15.769671	0.04	0.07	1.42	0.21	1.0	0.86	2.82	1.9	51.95	30.66	104.42	543.62	0.00616
R 119801	24.17634	15.804625	0.11	0.15	0.0	0.35	1.0	0.72	1.86	1.37	49.06	48.9	163.92	2180.65	0.00393

Notes.
[a] Selected nearly embedded cluster candidates from M. Rodríguez et al. (2025). See Section 3.2 for selection criteria. The flux values in this table are ratios using Janskys, normalized to the F200W filter. The values have not been corrected for extinction, since we do not have $E(B-V)$ values from an SED fit using the HST data in most cases.
[b] The 2.0 flux in mJanskys can be used to convert the relative flux values in this table to absolute values.

circles in the figure. The other (M. Rodríguez et al. 2025) clusters are not shown, but their photometric characteristics are listed in Table 5.

A careful look at Figures 8 and 9 show that, in most cases (10 of 12), the nearly embedded cluster can be seen as a very faint reddened object(s) in the IVB image. However, H 516 and H 1000 appear to be associated primarily with bluish optical sources, with no faint reddened objects associated with them.

Another important result is that, in nearly all cases (11 of 12), there is a relatively bright blue cluster within a few tenths of an arcsec. The only exception is H 1076, and even then there are two bright clusters roughly $0\farcs7$ away. This suggests that the formation of most nearly embedded clusters was triggered by a young nearby (10–30 pc) star cluster. In four of the cases, the nearby blue cluster is in the HST human-based cluster catalog (D. Maschmann et al. 2024) as a class 1 or 2 object with a young age (i.e., H 368–4 Myr, H 516–3 Myr, H 538–4 Myr, and H 572 3 Myr), as determined by D. Thilker et al. (2025).

In several cases, a dark brick-like dust feature appears to be associated with the nearly embedded cluster candidate, as generally seen best in the IVB image. Perhaps the best examples of this morphology are H 319, H 368, H 442, H 447, H 538, H 572, H 932, and H 1076 (especially the H_α image for this object).

Other things to notice include the following: (1) the objects are quite prominent in all three of the emission bands (somewhat less so in F335M) and generally have similar morphology that are most like the 1 and 2 Myr training objects in Figure 5; (2) in the F200W filter, the clusters are generally seen as fairly prominent, fuzzy objects, often with multiple point-like sources associated with them; and (3) the contrast with the very crowded background around the central F200W source is quite low in many cases, implying that the uncertainty in the photometry may be larger than in most other filters (e.g., H 338, H 572, and H 1000).

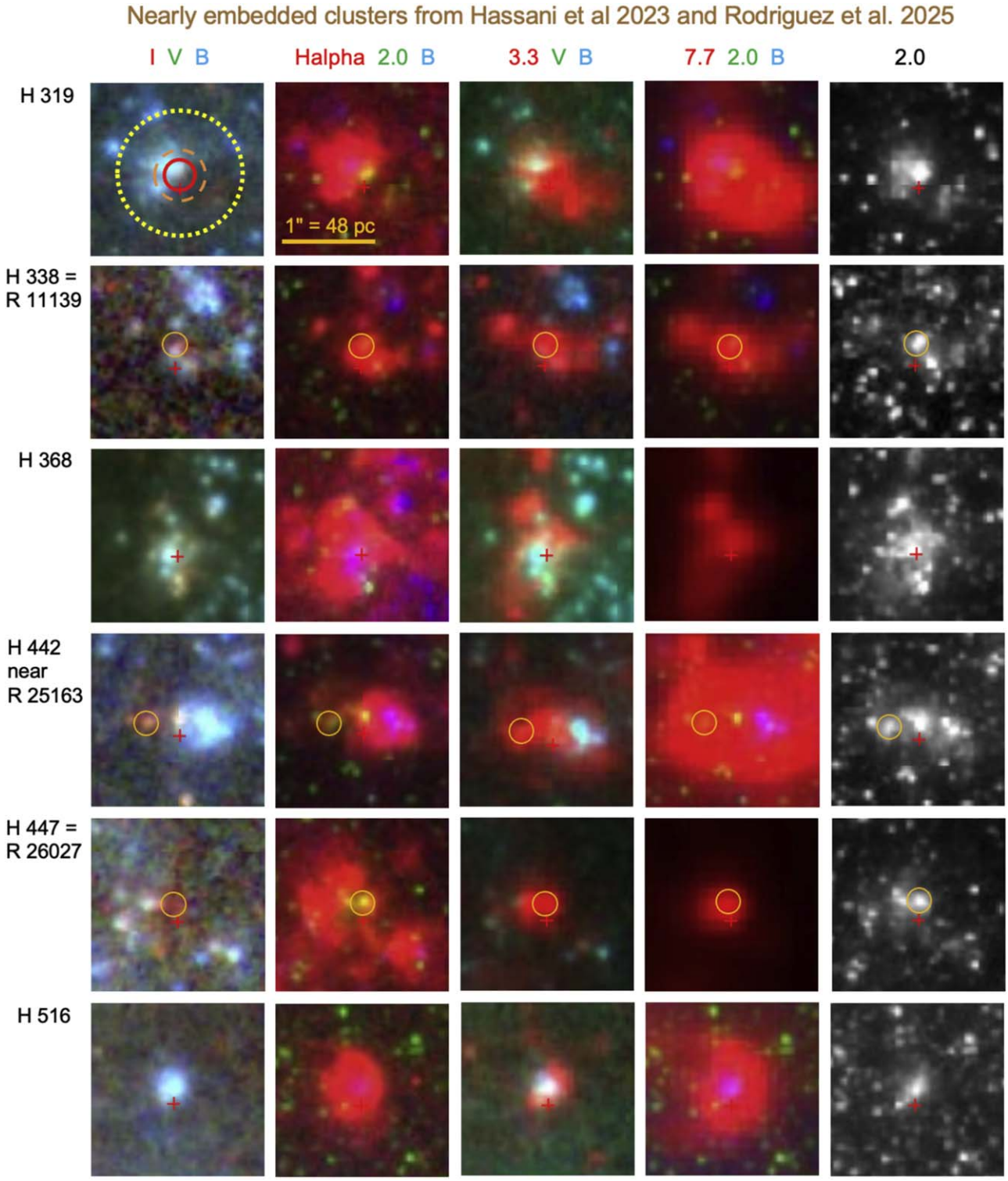

Figure 8. The first 6 of 12 nearly embedded cluster candidates from H. Hassani et al. (2023) (ID numbers starting with H and taken from the Hassani catalog). Four of the clusters are also either coincident with or near embedded cluster candidates from M. Rodríguez et al. (2025), as shown by the small yellow circles (labeled with ID numbers starting with R and taken from the Rodriguez catalog). See text for selection criteria and discussion. The filters used to produce the images are indicated above the top row. The photometric field of view used for nonconvolved (i.e., small-aperture) photometry used for the training clusters and for M. Rodríguez et al. (2025) photometry are shown in the first panel (i.e., red circles for optical and NIRCAM; orange dashed line for F770W; yellow dotted line for F2100W image). The large-aperture convolved photometry used by H. Hassani et al. (2023) uses the yellow dotted line aperture for all wavelengths. The scale is shown in the top row. The H. Hassani et al. (2023) program object is 5 pixels above the small red cross in all cases.

We show the SED flux measurements for both the H. Hassani et al. (2023) and M. Rodríguez et al. (2025) samples in Figure 10, which is similar to Figure 7 but now normalized at F200W, since some of the nearly embedded clusters are not well detected in the F814W filter. These clusters have optical broadband and H_α (only available for the Rodriguez sample) flux measurements that are lower than the optically based templates in Figure 10, as expected for clusters with high

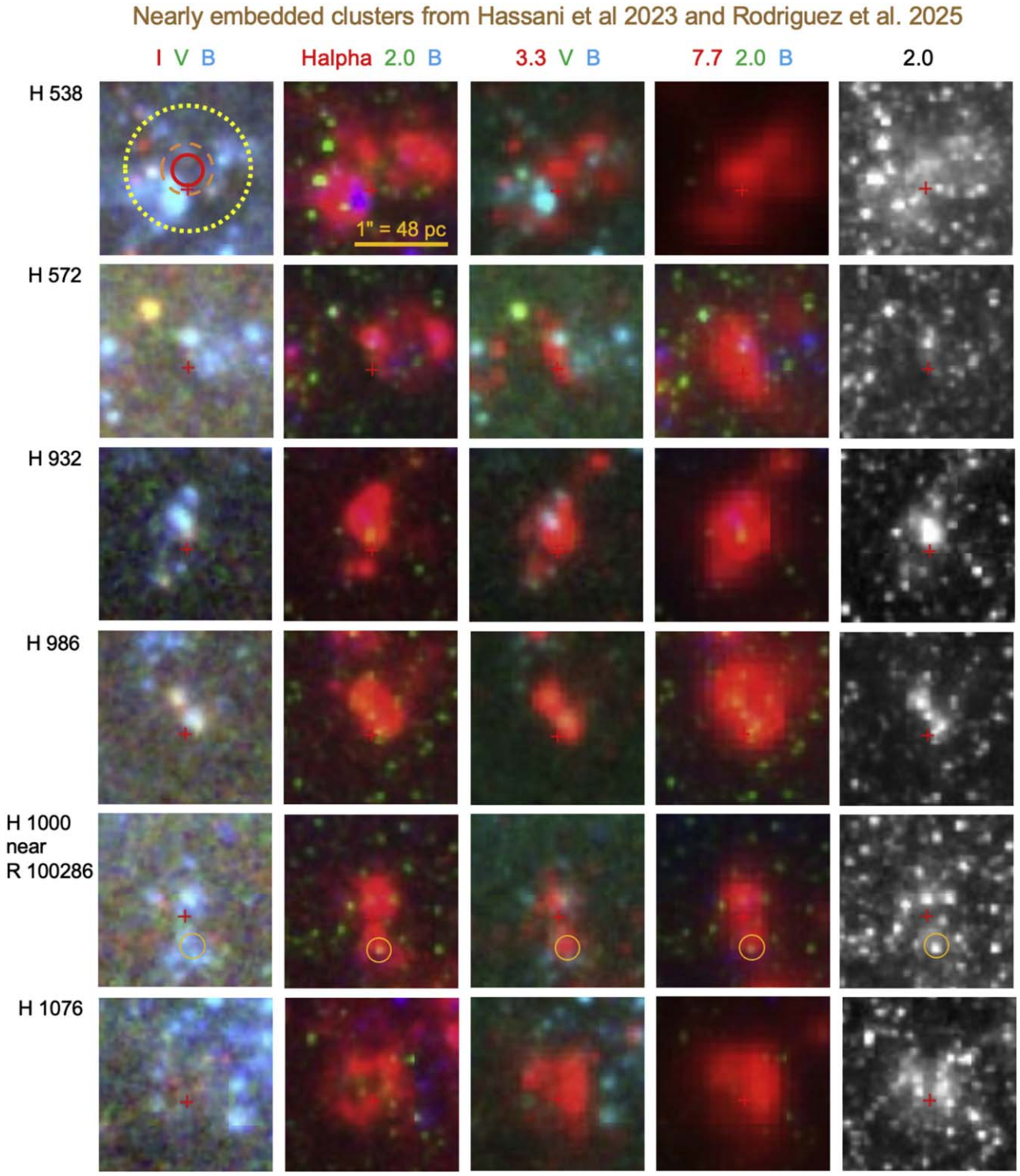

Figure 9. Same as Figure 8, for the last six nearly embedded cluster candidates.

extinction (which we cannot correct for, since we do not have $E(B-V)$ values from age-dating in the optical).

We find that the M. Rodríguez et al. (2025) *nearly embedded cluster candidates have essentially the same infrared SEDs as the 1–3 Myr clusters from our optically identified training set*. This is consistent with the results from M. Rodríguez et al. (2025), who find that the subsample of 3.3 μm-enhanced clusters with no HST emission have very similar SED profiles to the subsample of 3.3 μm-enhanced clusters that do have HST emission.

The H. Hassani et al. (2023) sample of nearly embedded clusters shown in the bottom panel looks similar, but has even smaller scatter, probably because the larger apertures (0.″67 radius) improve the signal-to-noise ratio, especially for the NIRCAM filters where a smaller 0.″124 radius aperture is used for the M. Rodríguez et al. (2025) sample.

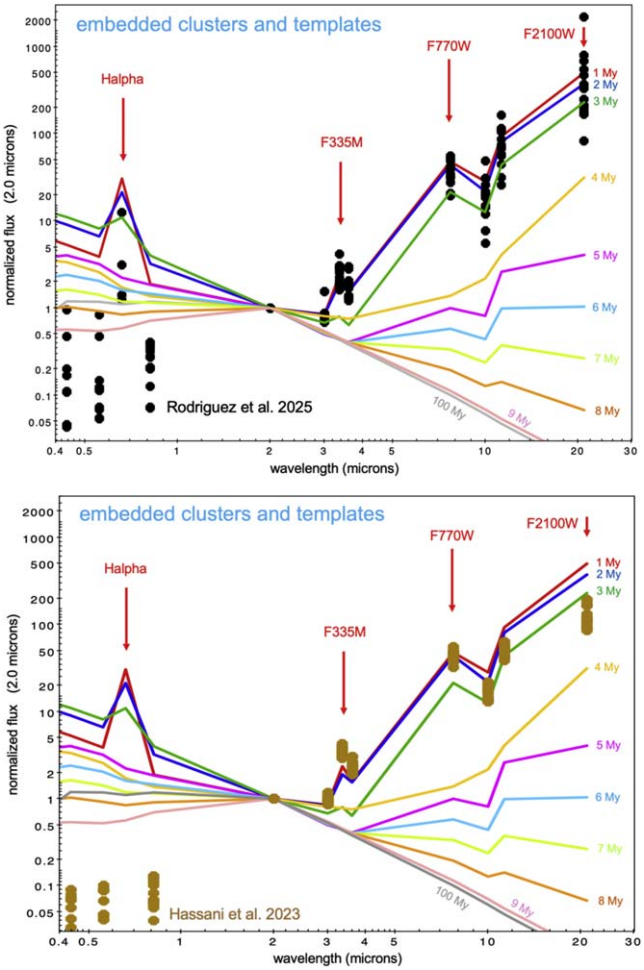

Figure 10. SEDs for nearly embedded cluster candidates compared to empirical templates based on optically identified clusters. The top plot shows data from the M. Rodríguez et al. (2025) sample using small-aperture photometry. The bottom plot shows data from the H. Hassani et al. (2023) sample using convolved large-aperture photometry. The same empirical templates as shown in Figure 7 are used, but are now normalized at 2.0 μm rather than F814W, since several of the nearly embedded clusters are very faint in the F814W filter. We find that the nearly embedded clusters have SEDs similar to the 1 to 3 Myr clusters in the optical training sample, and the convolved photometry results in slightly shallower SED slopes in the mid-IR.

The use of different apertures (i.e., "small-aperture" photometry for M. Rodríguez et al. (2025); large "convolved" aperture photometry for H. Hassani et al. (2023)—see discussion in Section 2.2.1) allows us to test how much effect this has on the resulting SEDs. The NIRCAM values are nearly identical, but we find a small, systematic change toward shallower slopes for the MIRI filters for the Hassani sample using convolved large-aperture photometry, reaching a difference of about a factor of three for the F2100W filter in Figure 10. This can be understood by the fact that the F2100W observation uses essentially the same aperture, while the F200W aperture has increased a factor of 5.4 in radius, or nearly 30 in area. As can be seen in a variety of images (e.g., Figure 8), there are typically several other clusters or stars within the 0.″67 aperture (shown as the yellow dotted line), hence the flux will be considerably larger for the F200W measurement, and hence the normalized value of F2100W/F200W used in the SED will be lower when using the large aperture. A similar result is obtained in Appendix B when comparing the convolved and small-aperture photometry for the training sample.

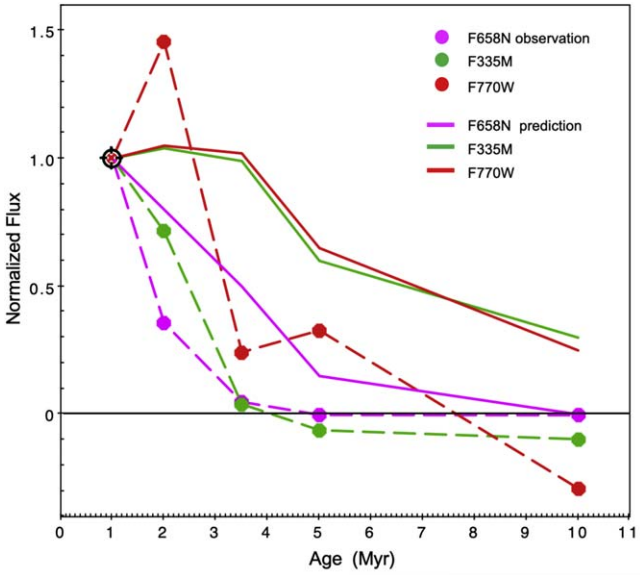

Figure 11. Observed and predicted evolution of H_α, F335M and F770W emission. The solid lines are from the predictions from the CIGALE/Draine models (see also Figure 7 in B. C. Whitmore et al. 2023b), which are static models that do not take into account outflows due to feedback. The dashed lines are from our empirical templates based on the observations, and have been normalized to 1.0 at an age of 1 Myr. In all cases, the observed profiles are much steeper than the predicted values, and they are nearly zero by 4 Myr for the F335M and H_α profiles.

While the factor-of-three difference between the top (small-aperture photometry) and bottom (convolved-aperture photometry) at F2100W is an important component, we note that the overall change in the F2100W flux is a factor of about 100 between a 1 and 5 Myr cluster, and hence is the dominant influence when estimating the ages of the clusters. See Appendix B for a similar comparison using the 40 clusters in the training sample.

3.3. Temporal Evolution of H_α, 3.3 μm, and 7.7 μm PAH Emission

In Figure 11, we use our mean-value empirical SEDs to plot the evolution of the 3.3 and 7.7 μm PAH band strength and compare them with the H_α evolution. The continuum flux has been estimated and subtracted using the mean of the F555W and F814W flux values for the H_α measurement, the F300M flux for the F335M measurement, and the F1000W flux for the F770W measurement. The 3 and 4 Myr points have been averaged together to reduce the scatter. As expected, based on our examination of Figures 5 and 6, the 3.3 and 7.7 μm PAH lines fall off quickly, and they essentially disappear by ∼5 Myr. This supports the primary result of this study, that stellar feedback can remove or destroy most of the gas and dust from the small apertures used for our study within just a few Myr.

We also note a similar evolution for Hα emission. This new result will be important for including H_α in future star cluster age-dating studies, since the presence of H_α is generally considered to be evidence of an age less than 7 Myr (e.g., C. Leitherer et al. 1999), rather than less than 4 Myr as found in the current study. While there are stars with enough UV flux to ionize the gas and hence produce H_α emission for ages around 5 Myr, it appears that the gas has already been removed from

the immediate area around the cluster by this age, resulting in few or no clusters with H_α emission in the 5–7 Myr age range. Hence, in both the H_α and PAH emission, the dominant physical mechanism responsible for controlling the temporal evolution appears to be the destruction or removal of the gas and dust.

As noted in Section 2.4, Figure 5 suggests that the 3.3 μm emission is weaker and more disjointed than H_α at a given age in a number of cases. Somewhat surprisingly, Figure 11 does not appear to be consistent with this interpretation, since the profiles look nearly identical for the two bands. A more careful treatment using a larger sample will be required to make a definitive determination of the relative temporal evolution of H_α and 3.3 μm in the future.

The longer-wavelength PAH features may last longer because they originate from larger dust grains (D. Baron et al. 2024). While Figure 11 provides some evidence for this at 7.7 μm, since there is still weak emission out to 5 Myr, it is difficult to make any conclusions at older ages based on our observations in the 7.7 and 11.3 μm PAH bands, since they reach the detection level at about 5 Myr. A few older clusters in Figure 6 appear to show some evidence of associated weak F770W emission (i.e., 3433 in the 5 Myr sample and 1187 and 4356 in the 10 Myr sample), but with such small-number statistics, this is very uncertain. Our future study of the larger sample will address this topic more carefully.

3.4. Color–Color Diagrams

With initial empirically based template SEDs in hand, we can now make optical-IR color–color diagrams similar to the UV-optical color–color diagrams that have been such a useful tool in the past. While other color combinations are possible, in this paper we only consider the F814W − F335M (i.e., *I* band —3.3 μm) versus F300M − F770W (i.e., 3.0–7.7 μm) diagram. Some advantages of this combination include the following: (1) F814W is the reddest optical band that is still detected for most nearly embedded clusters, hence including this filter provides the widest possible wavelength baseline; (2) the use of continuum (F814W and F300M) and PAH bands (F335M and F770W) in each axis helps separate the young and old objects, with a spread of ≈5 or 6 mag in each color over the age range from 1 Myr through 10 Myr; and (3) F770W is the shortest-wavelength MIRI band in our data set and hence has better spatial resolution than the other MIRI filters at longer wavelengths. The ABmag system is used for this figure.

Figure 12 includes the colors for 37 of the 40 clusters in the training set (i.e., from Table 1—excluding the three clusters discussed as outliers in Section 2.5) plotted as color-coded filled circles in the figure; the empirical SED templates using mean values derived in this paper (black line and small black dots showing various ages); the empirical SED templates using the BC03 stellar-continuum values for the NIRCAM filters for ages greater than 3 Myr (i.e., dashed black line showing the lower-limit templates as discussed in Section 3); and the nearly embedded clusters from M. Rodríguez et al. (2025) as open red squares. The H. Hassani et al. (2023) sample of nearly embedded clusters is not included, since it uses a different photometric methodology (i.e., convolved images matched to the 0.″67 F2100W resolution) and hence cannot be put precisely on this diagram. As expected, the youngest clusters, with strong F335M and F770W emission, tend to show up in the upper left part of Figure 12 (i.e., the red—1 Myr and blue—2 Myr circles, as well as all the embedded objects). The older clusters, e.g., 10 Myr (pink), 150 Myr (cyan), and 500 Myr (gray), tend to be in the bottom center part of the diagram.

We note that the scatter in the observed data points for the 3 (green), 4 (yellow), and 5 (maroon) Myr data points is much larger than the 1 (red), 2 (blue), and 10 Myr (pink) data points. This is most likely due to the very irregular, often patchy bubble morphologies of the 3 through 5 Myr clusters, as seen in Figures 5 and 6. Anticipating the discussion on the TODDLERS models (A. U. Kapoor et al. 2023) in Section 4.1, this also may reflect the "looping" nature of the colors in this age range. The relatively large difference between the empirical templates using the mean (solid black line) versus BC03 stellar-continuum models for 4–8 Myr (dashed black lines) also reflects this larger scatter and difference in morphology. A larger training set in the future should help clarify whether this is primarily observational scatter, or an inherent difficulty in age-dating objects in this age range, due to differences in morphology.

All of the M. Rodríguez et al. (2025) nearly embedded cluster candidates (red squares) appear to the left of even the youngest clusters in the training set. This is primarily due to large values of extinction and reddening that have not been corrected, because most of these objects do not have age estimates from HST and hence do not have measured $E(B-V)$ values, unlike the other points in the figure.

The brown line in Figure 12 represents an implementation of the B. T. Draine et al. (2021) models in the CIGALE framework that K. F. Henny et al. 2025 found matched the observational data in NGC 628 relatively well for very young clusters. It has A550 = 1.0 mag, $Q_{\rm pah} = 0.65$, $\alpha = 2.0$, and $f_{\rm esc} = 0.8$. Note that, while there is good agreement between the 1 and 2 Myr predictions and the observed training set points, there is a dramatic difference for older clusters. This discrepancy is probably due to the fact that the ISM is removed or destroyed from the immediate vicinity of a cluster on short timescales, making the assumption of energy balance used in the current implementation of the B. T. Draine et al. (2021) models in the CIGALE framework (M. Boquien et al. 2019) inappropriate for older clusters.

4. Discussion

4.1. Comparison with Predictions from TODDLERS Models

The SED models in the TODDLERS library developed by A. U. Kapoor et al. (2023) are designed specifically for the dynamic situation around a young star cluster, as they follow a homogeneous gas cloud as it evolves due to stellar feedback processes such as stellar winds, radiation pressure, and supernovae.

The bottom left panel of Figure 19 from A. U. Kapoor et al. (2023) shows the resulting UV-through-mm SED for a model with solar-metallicity clouds, number density $n_{\rm cl} = 80\ {\rm cm}^{-3}$, and a star-forming efficiency of 5%. Models with ages 0.1, 0.5, 1, 2, 5, 7, and 10 Myr are included. The models are in relatively good agreement with our empirical templates shown in our Figure 7, with rapidly rising flux values in the mid-IR for the first few Myr, but much flatter SEDs for ages 5 Myr and older.

A more detailed comparison can be made from the color–color diagram in Figure 13, with nine TODDLERS models shown in orange. The models show a number of remarkable similarities with our empirical templates shown in black (solid

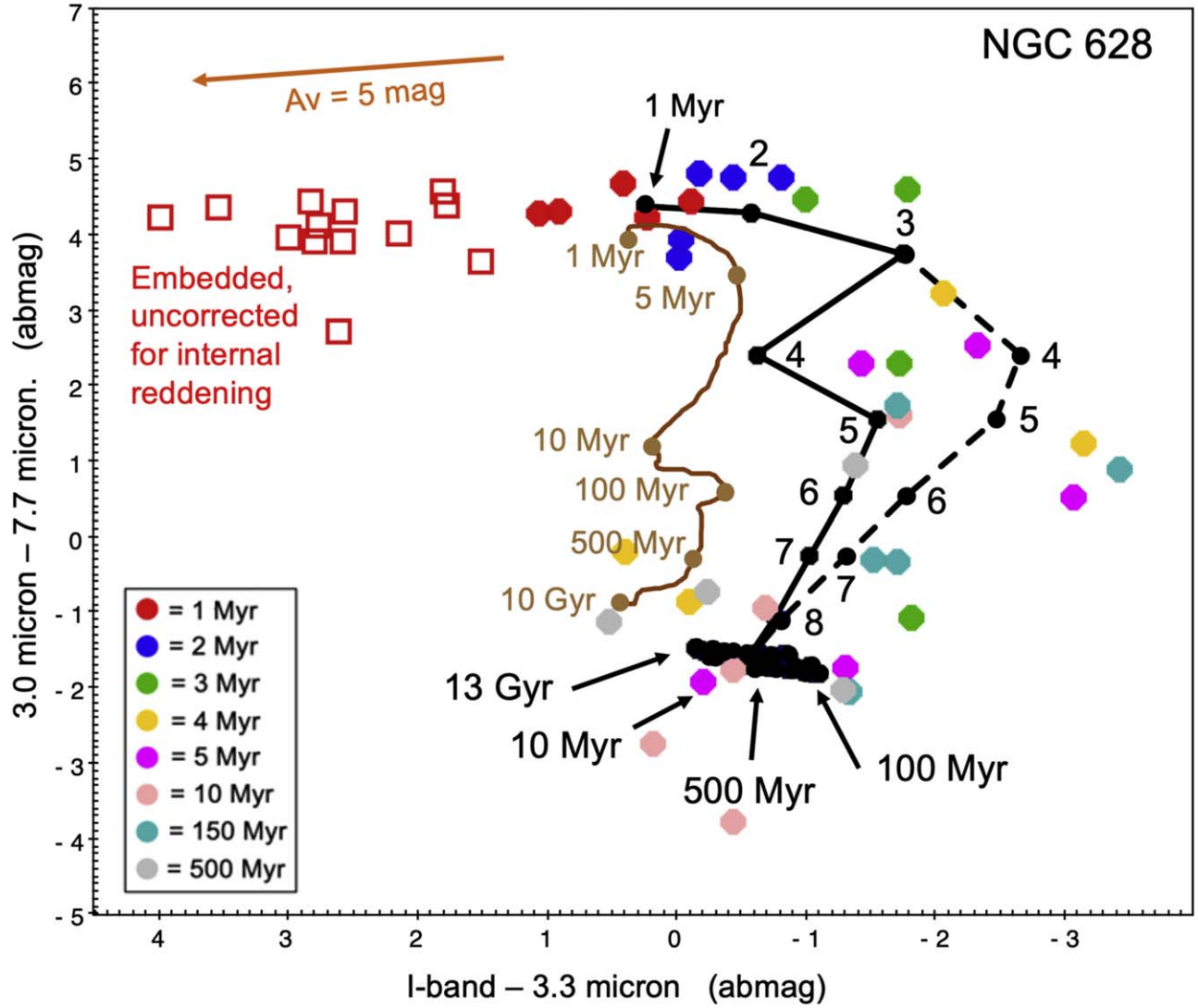

Figure 12. An I—3.3 μm vs. 3.0–7.7 μm diagram for our training set (color-coded filled circles). The black line is the empirical template based on our training set using means out to 8 Myr, with ages marked by black dots. The dashed black line shows the version with the BC03 stellar continuum used in the near-IR for ages in the 4–8 Myr range (i.e., the lower-limit template; see text for discussion). The brown line is a CIGALE/Draine model from K. F. Henny et al. 2025, as discussed in the text. Note that there is good agreement for the 1 and 2 Myr predictions but a dramatic difference for older clusters. The red squares are the nearly embedded clusters from M. Rodríguez et al. (2025) discussed in Section 3.2. Unlike the other data points, they have not been corrected for reddening. A reddening vector with $A_V = 5$ mag is shown in orange.

line for the version using means out to 8 Myr; dashed line for version using the stellar continuum for NIRCAM bands from 4 to 8 Myr), with the large color-coded filled circles showing the training sample, as discussed in Figure 12. One of the models that shows the best resemblance is included in the center of the figure. It has $n = 40\,\mathrm{cm}^{-3}$, SFE = 0.075, $M = 10^6\,M_\odot$, and $z = 0.02$ (i.e., solar metallicity).

A grid of TODDLERS models covering a range including $n = 10$, 40, and $160\,\mathrm{cm}^{-3}$ and SFE = 0.025, 0.075, and 0.125 around this central model is included using orange crosses and lines, with age estimates from 0.1 (the black open circle) to 10 Myr labeled in orange.

Several TODDLERS models show good agreement with the observations and empirical templates in three respects: (1) the position of the 1 Myr clusters in F814W − F335M versus F300M–F770W color–color space; (2) the positions of the 2 to 5 Myr clusters, although some show a roughly linear progression while others show a looping (in color–color space) evolution in this age range; and (3) the position of clusters older than 10 Myr (i.e., as predicted by the BC03 stellar-continuum models).

We also note that several aspects of the models vary dramatically, providing good diagnostic power. These include the following: (1) the youngest (0.1 Myr) models have F335M emission that is much too strong (left) in F814W − F335M for all the $n = 160\,\mathrm{cm}^{-3}$ models; (2) there are large gaps (rapid evolution) between certain young and old ages (e.g., between 1.7 and 2 Myr in the central panel); and (3) the location of the intermediate age (6–8 Myr) clusters swings rapidly from F814W − F335M = −2.0 to 0.0 as a function of SFE for the $n = 40$ and $160\,\mathrm{cm}^{-3}$ models.

While the good correspondence between some of the TODDLERS models and the empirical templates is encouraging, it is not the main focus of this pilot study, hence we leave a more detailed comparison for the future when more accurate empirical templates are available. We are also investigating the incorporation of the TODDLERS library of SED models, as well as some aspects of the empirical templates discussed in the

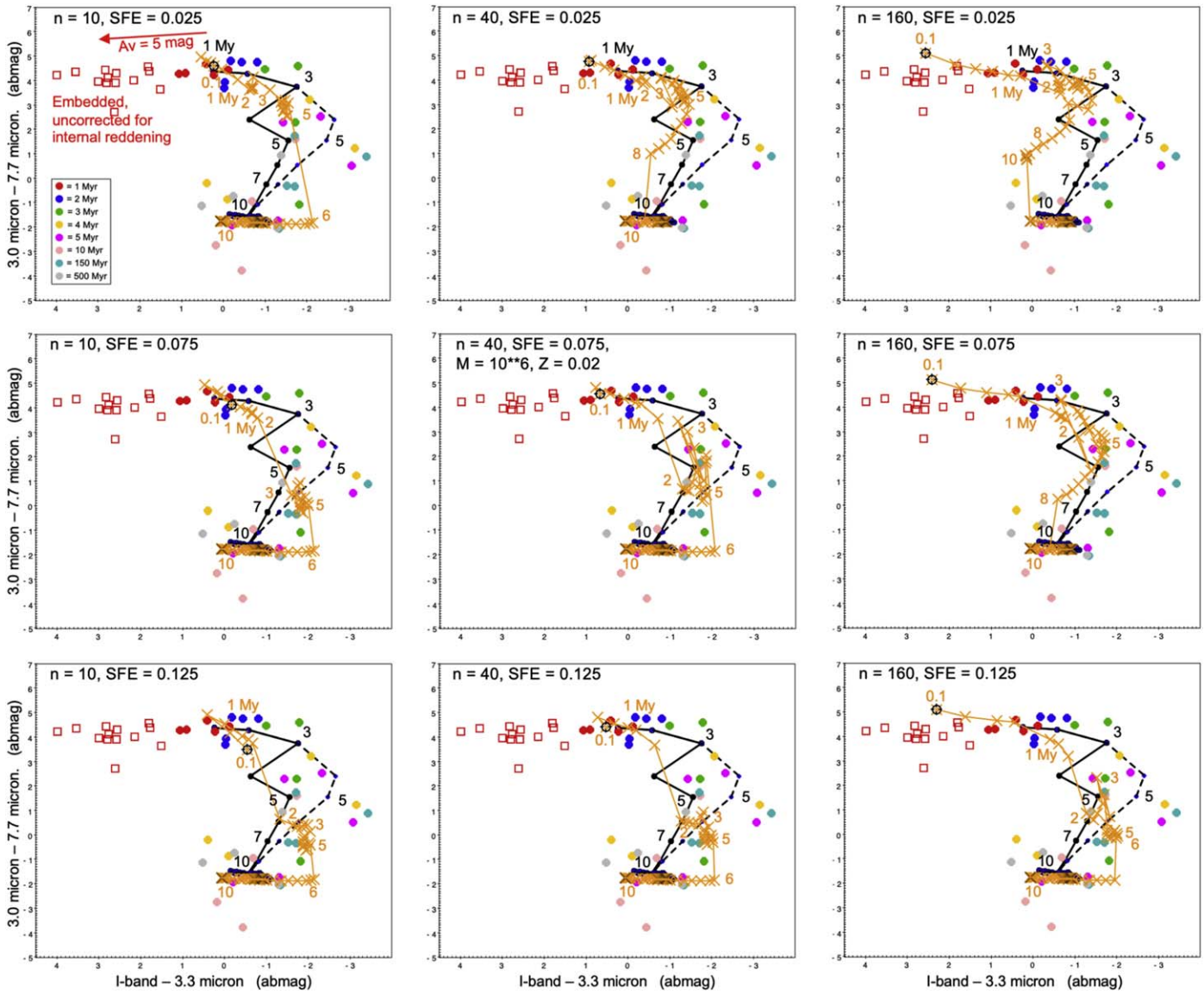

Figure 13. Similar to Figure 12, but overplotting a grid of TODDLERS (A. U. Kapoor et al. 2023; orange crosses and ages) models covering a range from $n = 10$, 40, and 160 cm^{-3}, with SFE = 0.025, 0.075, and 0.125, around a central model that shows relatively good agreement with the empirical template models. A model age of 0.1 Myr is shown by the black open circles.

current paper, into CIGALE (M. Boquien et al. 2019) in the future.

4.2. Comparison with Related Observational Work

One of the primary results from our study is that only star clusters with ages less than about 5 Myr have strong PAH or infrared dust continuum emission. A similar result has also been reported in M. J. Rodríguez et al. (2023) based on selection of cluster candidates using the 3.3 μm image. They found that most of the 3.3 μm emitters have ages less than 2 Myr.

The slightly older limiting age found in the current study may be due to the use of SEDs that include MIRI observations out to 21 μm, and hence may reflect the slower destruction of the larger dust grains responsible for the 7.7 through 21 μm emission compared to the 3.3 μm emission (O. V. Egorov et al. 2023; J. Chastenet et al. 2023; K. M. Sandstrom et al. 2023). However, the M. J. Rodríguez et al. (2023) result might also be a slight underestimate due to the 1 Myr bias in the J. A. Turner et al. (2021) ages, as discussed in M. Rodríguez et al. (2025) and D. Thilker et al. (2025). The more recent M. Rodríguez et al. (2025) paper finds that most of the 3.3 μm emitters have ages less than about 3 Myr.

A related result is the finding that PAH emission is suppressed in H II regions (E. Churchwell et al. 2006; M. Relaño & R. C. Kennicutt 2009; O. V. Egorov et al. 2023; J. Chastenet et al. 2023; K. M. Sandstrom et al. 2023). It seems likely that both our result that most clusters with ages greater than 5 Myr do not have strong PAH or IR dust continuum emission and the results on suppressed PAH emission in H II regions are caused by a combination of the same two physical mechanisms, i.e., (1) the removal of gas and dust in the central region of superbubbles, due to outflows from the star cluster, and (2) the destruction of dust grains, resulting in the reduction of PAH emission. The relative importance of the two effects may depend on what size aperture is used for the observations.

In the current study, the focus is on determining ages of the star clusters, rather than investigating the nature of the H II regions around the clusters. There are relatively few studies that have examined PAH and IR emission from the star clusters themselves in external galaxies. However, two studies based on Spitzer observations suggest that PAH emission may be associated with clusters with ages in the range of tens or even hundreds of Myr (Z. Lin et al. 2020; K. Mallory et al. 2022). This would be in contradiction to the results from the current paper. It is possible that some of these cases are superpositions, since the initial selection of the sources in these studies is based on detection of IR emission in Spitzer observations, and the subsequent matching with the star cluster is based on position within the relatively large Spitzer PSF. JWST observations of these objects should provide a more definitive determination of whether the IR emission is actually associated with the older clusters or is randomly situated in these cases.

A number of other studies have also established a link between older stellar populations and PAH emission, including B. T. Draine et al. (2021) and A. K. Leroy et al. (2023). It is important to note that these results are for integrated stellar populations over a relatively large field of view—for example, parts of the bulge in M31 in the case of B. T. Draine et al. (2021), or the diffuse dust lanes in PHANGS galaxies in the case of A. K. Leroy et al. (2023). The results from the current study are primarily relevant for cases where individual star clusters have been observed using small apertures.

A recent study by A. Pedrini et al. (2024), taken as part of the Feedback in Emerging Extragalactic Star Clusters (FEAST) project (A. Adamo et al. 2025, in preparation), and also based on HST+JWST observations of NGC 628, finds several similar results and hence supports some of the basic conclusions from the current paper. There are, however, some important differences. A. Pedrini et al. (2024) find that strong PAH emission is only found in clusters younger than 7 Myr, with the most common ages being in the 3–6 Myr range. In the current paper, we find that strong PAH emission is only found for clusters less than about 5 Myr old, with the most common emission being in the 1–2 Myr range. While the details of the age-dating are not yet available for the FEAST study, it is likely that the primary difference is due to our use of a new and largely independent age-dating approach, as described in Section 2.

Another result of the A. Pedrini et al. (2024) study is the finding that the 3.3 and 7.7 μm bands have very similar temporal profiles (their Figure 9), while we find that the 3.3 μm band declines faster than the 7.7 μm profile, as shown Figure 11. While this remains an open question, a variety of recent observational results (O. V. Egorov et al. 2023; J. Chastenet et al. 2023; D. Baron et al. 2024) suggest fast destruction of the smaller grains responsible for the 3.3 μm PAH emission is commonly found.

5. Summary and Conclusions

In this pilot study, we use new infrared PHANGS-JWST NIRCAM and MIRI imaging of the spiral galaxy NGC 628 in the F200W, F300M, F335M, F360M, F770W, F1000W, F1130W, and F2100W filters, in addition to existing HST observations in the F275W, F336W, F438W, F555W, F658N, and F814W filters, to produce empirical SED templates for star clusters. These templates can be used both to provide age estimates for star clusters, and to test new models such as the TODDLERS SED library developed by A. U. Kapoor et al. (2023). Our primary conclusions are provided below.

1. Nearly all star clusters with strong PAH and IR dust continuum emission have ages in the 1–4 Myr age range (also see M. J. Rodríguez et al. 2023 and M. Rodríguez et al. 2025). In nearly all cases where there is strong PAH emission, there is also strong Hα emission.
2. In this pilot study, we develop empirical SED templates based on a carefully chosen training set of 40 clusters in NGC 628, ranging in age from 1 to 500 Myr, with masses greater than $\approx$3000 $M_{\odot}$. When combined with stellar-continuum models from BC03 models, which agree with observations of all clusters with ages greater than 10 Myr, we are able to provide SED templates for clusters of all ages.
3. Using these templates we plot the observed evolution of Hα and PAH (3.3 and 7.7 μm) strength and demonstrate that they are similar and all decrease rapidly (within a few Myr), but with the PAH 3.3 μm emission dropping faster than the 7.7 μm emission and possibly faster than Hα. These differences are likely influenced by the rapid destruction of small dust grains responsible for the 3.3 μm emission.
4. The rapid decline of PAH and IR dust continuum emission with age is probably due to a combination of the destruction of the dust grains and stellar feedback removing the gas and dust from the immediate vicinity of the star cluster. The timescale for the latter mechanism is compatible with dynamical estimates based on CO superbubble expansion velocities from E. J. Watkins et al. (2023) in NGC 628.
5. Samples of nearly embedded cluster candidates in NGC 628 from H. Hassani et al. (2023) and M. Rodríguez et al. (2025) are examined and found to have SEDs and colors very similar to the 1–3 Myr clusters from the optical training set in the IR part of the spectrum. The Hassani sample shows less scatter, and it is most consistent with the 1 Myr convolved-aperture template. In nearly all cases, we find there is a young star cluster within a few tenths of an arcsec (10–30 pc) of the nearly embedded cluster in the Hassani sample, suggesting the formation of the embedded object was triggered by its presence.
6. Using these empirical templates, we produce evolutionary tracks for the 0.8–3.3 μm versus 3.0–7.7 μm color–color diagram that are in agreement with the optically selected training set, the samples of nearly embedded cluster candidates, and the current implementation of the Draine models within CIGALE for ages of 1–2 Myr. For ages older than about 5 Myr the CIGALE/Draine models overpredict the strength of the PAH and thermal dust emission, probably due to the assumption of energy balance.
7. We find that the empirical SED templates are in fairly good agreement with the TODDLERS (A. U. Kapoor et al. 2023) SED model library, which is based on the dynamic, spherical evolution of a homogeneous gas cloud around a young stellar cluster. The model SEDs support our results that PAH and dust continuum emission dominates in the near-IR for only the first few Myr, and emission in the mid-IR is dominated by the stellar continuum after roughly 5 Myr.

In this pilot study, we report on results for a single galaxy (NGC 628, which is located at 9.84 Mpc), and a specific set of small apertures used for the HST and JWST photometry. We briefly examine the effects of using images convolved to the size of the F2100W point-spread function (0.″67) and find that it is an important but not dominant effect. We caution the reader that our quantitative results depend at least somewhat on these specific properties and assumptions, although we believe that the main conclusions are robust regardless of the specific details. These issues will be explored more fully in the future, when a much larger cluster sample will be used to determine higher-quality empirical SED templates for star clusters.

Acknowledgments

This work is based on observations made with the NASA/ESA/CSA James Webb Space Telescope (program #2107) and the NASA/ESA Hubble Space Telescope (program #15654 and #13364). The data were obtained from the Mikulski Archive for Space Telescopes at the Space Telescope Science Institute, which is operated by the Association of Universities for Research in Astronomy, Inc., under NASA contract NAS 5-03127 for JWST and 5-26555 for HST.

We thank the referee for a careful reading of the paper and several suggestions that greatly improved the paper.

A.W. acknowledges UNAM's DGAPA for the support in carrying out her sabbatical stay at UCSD, USA, through program PASPA.

K.G. is supported by the Australian Research Council through the Discovery Early Career Researcher Award (DECRA) Fellowship (project number DE220100766) funded by the Australian Government. K.G. is supported by the Australian Research Council Centre of Excellence for All Sky Astrophysics in 3 Dimensions (ASTRO 3D), through project number CE170100013.

M.B. gratefully acknowledges support from the ANID BASAL project FB210003 and from the FONDECYT regular grant 1211000.

This work was supported by the French government through the France 2030 investment plan managed by the National Research Agency (ANR), as part of the Initiative of Excellence of Université Côte d'Azur under reference number ANR-15-IDEX-01.

M.C. gratefully acknowledges funding from the DFG through an Emmy Noether Research Group (grant number CH2137/1-1).

Data Availability

The imaging observations underlying this article can be retrieved from the Mikulski Archive for Space Telescopes at https://archive.stsci.edu/hst/search_retrieve.html under proposal GO-15654. High-level science products, including science ready mosaicked imaging, associated with HST GO-15654 are provided at https://archive.stsci.edu/hlsp/phangs-hst. The specific PHANGS-JWST observations analyzed can be accessed via doi:10.17909/9bdf-jn24, and the PHANGS-HST images can be accessed via doi:10.17909/t9-r08f-dq31. The full version of the empirical templates (both the mean-value and the lower-limit versions) can be accessed via doi:10.17909/jray-9798.

Facilities: HST, JWST, ALMA.

Software: ASTRODENDRO, AstroPy, CIGALE, Photutils, TOPCAT.

Appendix A
A Closer Look at the 1–4 Myr Box

Figure 14 provides a more detailed look at the 45 (of 58) clusters within the 1–4 Myr box that fall within the field of view of the F770W image. Thirty-one of these 45 clusters have strong PAH emission, defined as F770W/F300M flux > 20, as in Figure 3. This figure supports several assumptions discussed in Section 2.3.1, and it provides additional insight into the youngest clusters.

The figure is broken into six classifications, which are shown for the strong PAH sample on the left and the weak PAH sample on the right. The sequence is roughly in order of age, with compact H_α objects on the left, followed by small superbubbles, clusters near the edge of the shell of superbubbles, and large superbubbles in the first four columns. Clusters that are more uncertain (e.g., possible superpositions) are in the fifth column, followed by clusters with no obvious H_α (just 2 of the 45) in the last column.

Clusters without O and B stars that are not massive enough (hot enough) to ionize hydrogen atoms are not expected to have H_α emission, and this is apparently the case for just two clusters (2446 and 4275). In two more cases (4460 and 5030), there is H_α in the area, but it is not clear whether it is associated with the cluster (i.e., no clear bubble or morphological shape that suggests a connection). This suggests that, in $27/31 = 87\%$ of the strong PAH sources, there is H_α associated with the clusters, in agreement with our discussion of Figures 1 and 2 in Section 2.1.

In general, the large bubbles have weak PAH emission, since most of the gas and dust has been blown outside the effective aperture used for our study (i.e., the orange dashed circle for the F770W and the dotted yellow circle for the F2100W effective aperture). We note that most of the weak PAH sources on the right side of Figure 14 also appear to have some H_α associated with them. Hence, the vast majority of all the clusters in the 1–4 Myr box are very young, as predicted based on the discussion of nondegenerate regions in Section 2.3.1. Finally, we note that there is a roughly even distribution of clusters from very compact ($\approx$1 Myr) to large bubbles and uncertain objects ($\approx$4 Myr), which was one of the assumptions used in Section 2.3.2.

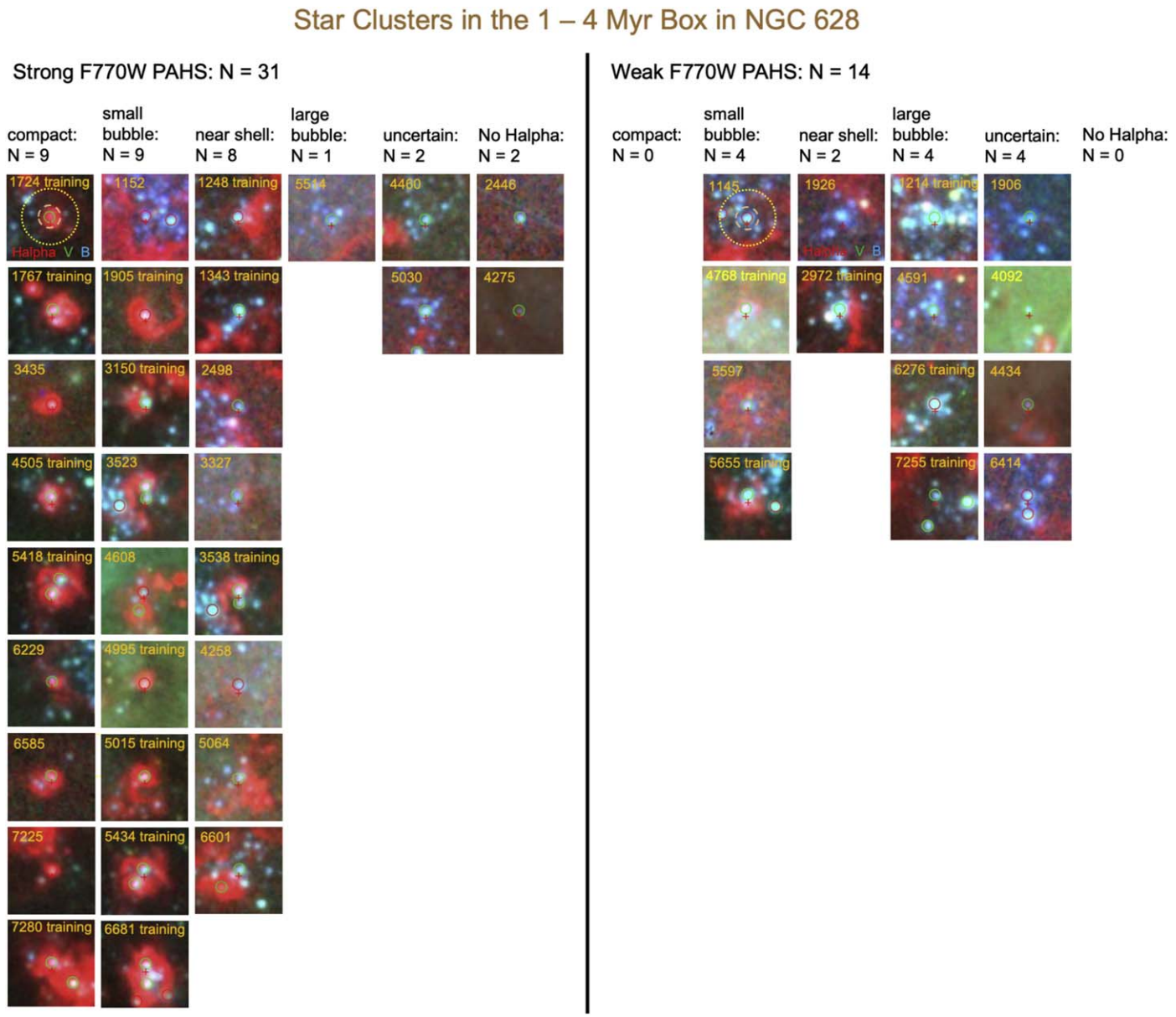

Figure 14. H_α, *V*, *B* images of the 45 sources within the F770W FOV in the 1–4 Myr Box. The 20 clusters included in the training set (i.e., highest-mass objects) are also identified in the snapshots. Red circles are used for class 1 clusters, while green circles are used for class 2 clusters. Aperture sizes, as included in Figure 4, are shown in the first panel.

Appendix B
Convolved Large-aperture Photometry of the Training Set

In Sections 2.2.1 and 3.2, we briefly discussed the use of convolved large-aperture photometry. In this appendix, we take a closer look at SEDs derived using convolved-aperture photometry from H. Hassani et al. (2023) of clusters in our optically selected training set, and compare with SEDs derived using the small-aperture photometry discussed in Section 2.2.1. The photometry used in this exercise is included in Tables 6 and 7.

Figure 15 shows a blowup of part of the bottom panel from Figure 10, this time including SEDs derived from photometry based on convolved images from H. Hassani et al. (2023) (i.e., the dashed color-coded lines). The first thing to notice is that the observations for the 12 nearly embedded cluster candidates discussed in Section 3.2 (the brown points) agree best with the SEDS derived from the convolved images for the 1 Myr clusters (i.e., the red dashed line). This is similar to the conclusion for the M. Rodríguez et al. (2025) nearly embedded cluster candidates using small-aperture photometry, although in that case (upper panel of Figure 10), there was also reasonable agreement with the 2 and 3 Myr templates for a few of the embedded clusters.

The next point to notice is that the convolved SED templates are systematically shallower than for the small-aperture templates for 1–3 Myr. This is to be expected, since the aperture used for the F2100W photometry is unchanged, but the size of the shorter-wavelength apertures are dramatically increased (e.g., from $0\farcs12$ to $0\farcs67$ for NIRCAM) in the case of the convolved apertures. Hence, they include surrounding clusters in many cases, thus increasing the F200W flux and reducing the ratio between F2100W and F200W (e.g., examine

Table 6
Normalized Flux Values Using Small-aperture Photometry for the Training Set[a]

ID[b]	Age[c]	0.275	0.336	0.435	0.555	0.658	0.814	2.0	3.0	3.3	3.6	7.7	10.0	11.3	21.0	0.814-flux[d]
1724	1.0	5.15	4.07	2.38	1.9	26.48	1.0	0.7	0.55	1.78	1.1	27.79	12.5	40.7	84.4	2.86
1767	1.0	4.08	3.27	2.06	1.5	20.35	1.0	0.72	0.53	1.64	1.08	26.78	14.9	49.0	224.1	14.10
4505	1.0	3.95	2.93	2.12	1.38	11.46	1.0	0.4	0.28	0.77	0.5	16.52	7.8	30.3	111.0	6.63
5418	1.0	4.88	3.79	2.39	1.83	11.6	1.0	0.49	0.35	0.92	0.61	17.15	8.3	29.6	166.9	6.68
7280	1.0	4.72	3.41	2.24	1.67	11.2	1.0	0.32	0.53	1.16	0.93	38.91	31.6	97.3	746.1	4.65
3150	2.0	4.44	3.52	2.47	1.73	2.79	1.0	0.18	0.14	0.33	0.22	11.15	4.6	21.2	85.1	14.11
3538	2.0	4.58	3.59	2.46	1.75	8.29	1.0	0.48	0.41	0.74	0.56	14.98	7.6	28.0	169.1	8.00
4995	2.0	4.18	2.89	2.09	1.56	8.56	1.0	0.28	0.16	0.62	0.45	13.65	6.0	21.6	80.7	3.66
5015	2.0	4.14	3.33	2.41	1.62	8.16	1.0	0.36	0.37	0.72	0.8	10.79	6.6	17.8	40.1	4.16
6681	2.0	4.33	3.29	2.34	1.59	5.24	1.0	0.28	0.22	0.53	0.37	17.38	9.1	36.8	207.7	8.22
1905	3.0	4.18	3.18	2.4	1.57	4.66	1.0	0.24	0.18	0.34	0.25	10.95	4.9	18.9	43.6	3.74
1343	3.0	4.34	3.14	2.2	1.51	1.26	1.0	0.44	0.19	0.14	0.12	−0.21	0.0	−0.4	1.4	12.5
2972	3.0	4.29	3.35	2.47	1.69	1.59	1.0	0.19	0.17	0.18	0.16	1.37	1.6	3.6	8.1	24.0
4768	3.1	4.33	3.16	2.04	1.54	2.48	1.0	0.81	0.3	0.31	0.28	0.29	−0.1	−0.1	7.4	7.41
5434	3.0	4.79	3.69	2.46	1.84	3.44	1.0	0.13	0.14	0.15	0.12	9.34	6.0	21.9	177.3	5.85
1214	4.0	1.78	1.66	1.42	1.07	1.06	1.0	1.4	1.42	1.43	1.41	1.18	3.4	3.3	4.6	31.2
1248	4.0	3.89	3.42	2.47	1.73	1.76	1.0	0.17	0.07	0.05	0.05	0.09	0.3	1.4	16.2	5.76
5655	4.0	4.8	3.91	2.64	1.88	1.0	1.0	0.19	0.13	0.12	0.1	2.47	1.7	6.4	71.2	13.8
6276	4.0	4.22	3.24	2.28	1.48	1.32	1.0	1.17	0.73	0.68	0.63	0.32	0.9	0.8	−0.1	32.5
7255	4.1	4.11	3.11	2.02	1.38	0.87	1.0	0.63	0.22	−0.07	0.03	−7.11	−3.1	−15.4	−6.9	3.45
1667	5.0	4.05	3.29	2.65	1.75	1.06	1.0	0.22	0.1	0.08	0.08	1.01	0.4	2.7	1.3	3.68
2416	5.0	1.45	1.42	1.44	1.15	1.03	1.0	1.36	0.73	0.65	0.6	0.12	0.7	0.5	0.5	19.7
3433	5.0	2.05	2.41	2.47	1.75	1.79	1.0	0.3	0.17	0.19	0.17	1.38	0.8	3.0	8.1	6.26
5894	5.0	1.52	1.31	1.53	1.22	1.04	1.0	0.67	0.3	0.25	0.22	0.06	0.2	0.2	−0.1	10.8
6895	5.0	2.93	3.04	2.81	1.98	1.37	1.0	0.12	0.05	0.03	0.02	0.14	0.1	0.7	1.3	5.47
1187	10.0	.88	1.23	1.1	0.96	0.99	1.0	0.91	0.4	0.32	0.27	0.16	0.0	0.2	0.1	12.0
2688	10.0	1.02	0.83	0.8	0.68	0.81	1.0	1.37	0.64	0.54	0.48	0.13	0.2	0.1	0.1	25.6
4356	10.0	0.94	0.79	0.67	0.58	0.49	1.0	2.02	1.05	0.89	0.8	0.18	0.7	0.5	0.7	9.61
5016	10.0	1.06	0.84	0.82	0.67	0.74	1.0	1.41	0.63	0.52	0.46	0.04	0.2	−0.1	−0.4	16.4
7150	10.0	1.11	1.08	1.03	1.06	1.26	1.0	0.35	0.16	0.14	0.12	0.68	0.4	1.8	1.4	10.2
1743	150.0	0.38	0.5	1.07	0.97	1.09	1.0	0.76	0.28	0.2	0.17	0.74	0.4	1.5	9.2	3.35
2535	150.0	0.29	0.45	0.98	0.99	1.01	1.0	0.61	0.27	0.2	0.19	1.31	0.7	2.4	1.0	2.80
4901	150.0	0.25	0.48	0.99	1.0	1.05	1.0	0.74	0.29	0.22	0.2	−1.43	−0.6	−3.2	−0.9	2.86
5736	150.0	0.23	0.38	0.91	0.89	0.94	1.0	0.61	0.3	0.2	0.17	−0.6	−0.7	−3.5	−3.6	2.74
6400	150.0	0.33	0.41	0.99	0.95	0.97	1.0	0.76	0.35	0.28	0.25	−0.09	0.0	−0.3	0.4	7.15
1516	500.0	0.16	0.23	0.83	0.84	0.85	1.0	2.77	1.41	1.46	1.43	0.49	0.6	0.7	0.2	3.09
2273	500.0	0.13	0.22	0.8	0.86	0.75	1.0	0.63	0.3	0.25	0.23	0.72	0.7	2.4	1.6	7.14
2352	500.1	0.06	0.2	0.67	0.94	2.54	1.0	0.63	0.35	0.46	0.35	8.3	3.9	16.7	45.7	8.98
2984	500.0	0.01	0.16	0.56	0.82	0.77	1.0	0.72	0.3	0.25	0.23	−0.06	0.2	−0.0	−1.0	3.75
6340	500.0	0.01	0.2	0.67	0.77	0.91	1.0	1.7	0.75	0.72	0.65	0.38	0.1	0.8	0.7	4.02

Notes.
[a] Small-aperture photometry from M. Rodríguez et al. (2025) for clusters in the training set, as defined in Section 2.2 and Table 1.
[b] Star Cluster ID # from D. Maschmann et al. (2024).
[c] Adopted age as discussed in Sections 2.3. The values with "0.1" attached are the outliers discussed in Section 2.5.
[d] The 0.814 flux in μJanskys can be used to convert the relative flux values in this table to absolute values.

Table 7
Normalized Flux Values Using Convolved-aperture Photometry for the Training Set[a]

ID[b]	Age[c]	0.275	0.336	0.435	0.555	0.814	2.0	3.0	3.3	3.6	7.7	10.0	11.3	21.0	0.814-flux[d]
1724	1.0	0.76	1.07	1.89	1.48	1.0	7.94	6.18	17.54	11.65	170.65	65.78	179.26	297.06	0.659
1767	1.0	0.44	0.66	1.35	1.16	1.0	4.77	4.06	13.27	8.87	170.36	77.19	210.48	724.12	3.890
4505	1.0	0.48	0.73	1.51	1.28	1.0	3.82	3.16	11.29	7.02	149.98	57.16	179.96	380.99	1.623
5418	1.0	0.44	0.66	1.4	1.17	1.0	3.35	2.48	7.52	4.99	94.19	34.1	105.32	300.53	2.744
7280	1.0	0.34	0.52	0.96	0.9	1.0	7.23	11.37	23.91	20.93	286.57	147.45	375.72	984.66	2.350
3150	2.0	0.48	0.74	1.47	1.31	1.0	4.72	4.13	11.81	7.99	152.38	48.96	179.95	345.81	2.744
3538	2.0	0.49	0.75	1.52	1.34	1.0	4.67	4.18	10.2	6.6	108.47	42.77	132.25	435.77	2.558
4995	2.0	−0.37	−0.46	−0.42	0.04	1.0	2.16	0.45	−4.24	−1.95	−114.35	−37.51	−135.77	−318.18	−0.806
5015	2.0	0.41	0.62	1.36	1.27	1.0	3.77	4.06	9.82	9.1	96.17	46.06	115.92	147.92	0.960
6681	2.0	0.47	0.69	1.45	1.29	1.0	3.78	3.04	9.59	6.21	125.84	45.96	146.55	366.24	3.421
1905	3.0	0.51	0.76	1.52	1.28	1.0	4.3	3.6	9.67	6.72	118.68	38.15	124.84	160.91	0.707
1343	3.0	0.65	0.83	1.72	1.39	1.0	2.51	1.21	0.71	0.76	−2.77	−1.49	−5.22	0.95	2.415
2972	3.0	0.42	0.66	1.46	1.3	1.0	4.61	4.42	4.68	4.22	8.92	9.41	13.99	23.17	6.860
4768	3.1	0.63	0.85	1.66	1.46	1.0	1.04	−0.13	0.69	−1.12	13.65	2.43	11.39	52.05	1.072
5434	3.0	0.38	0.57	1.19	1.13	1.0	4.23	2.86	6.49	4.45	79.04	29.57	87.06	278.79	2.746
1214	4.0	0.2	0.34	0.94	0.88	1.0	5.43	5.82	5.49	5.84	2.06	15.78	9.69	18.18	7.631
1248	4.0	0.46	0.74	1.66	1.41	1.0	1.43	0.56	0.17	0.52	6.56	0.56	3.01	51.91	1.256
5655	4.0	0.4	0.62	1.39	1.22	1.0	4.0	2.47	4.12	3.19	42.77	16.31	51.25	159.74	5.160
6276	4.0	0.59	0.82	1.72	1.36	1.0	6.61	4.69	4.47	4.24	0.24	4.98	2.23	6.63	4.642
7255	4.1	0.36	0.45	1.23	0.99	1.0	4.06	2.36	−1.12	0.24	−38.48	−10.5	−46.43	8.2	1.281
1667	5.0	0.82	1.12	2.07	1.77	1.0	5.33	2.68	3.48	2.41	28.03	12.64	38.49	9.52	0.457
2416	5.0	0.2	0.35	1.03	0.97	1.0	8.23	4.99	4.39	4.16	−1.75	4.85	0.9	1.04	2.578
3433	5.0	0.36	0.71	1.65	1.4	1.0	2.12	1.66	2.94	2.03	22.31	9.17	28.56	34.19	1.030
5894	5.0	0.17	0.28	1.02	0.95	1.0	3.87	1.97	1.61	1.43	−0.14	1.11	0.67	−2.73	1.899
6895	5.0	0.65	0.98	2.18	1.67	1.0	−0.32	−0.42	−0.23	−0.28	6.98	2.06	9.35	4.59	0.977
1187	10.0	0.23	0.3	0.81	0.78	1.0	5.72	2.68	2.39	2.1	4.18	1.11	4.62	3.87	1.999
2688	10.0	0.15	0.23	0.63	0.64	1.0	7.95	4.29	3.66	3.32	0.41	1.31	0.36	2.43	3.369
4356	10.0	0.11	0.18	0.44	0.43	1.0	10.16	5.56	4.9	4.56	1.6	3.8	2.65	1.84	2.542
5016	10.0	0.16	0.23	0.67	0.65	1.0	7.67	3.93	3.26	2.9	−0.6	0.89	−1.71	−0.58	2.436
7150	10.0	0.21	0.35	1.08	1.07	1.0	1.53	0.87	1.12	0.77	10.12	4.47	16.59	6.66	1.906
1743	150.0	0.14	0.22	0.84	0.86	1.0	4.81	2.64	3.48	2.5	37.29	12.54	32.84	30.53	0.851
2535	150.0	0.04	0.11	0.7	0.81	1.0	3.41	1.73	1.14	1.04	18.13	5.0	22.8	1.1	0.449
4901	150.0	0.05	0.13	0.69	0.81	1.0	2.17	0.9	0.49	0.69	−12.48	−4.26	−18.57	−5.95	0.724
5736	150.0	0.04	0.11	0.7	0.89	1.0	3.65	1.6	0.99	0.38	−10.97	−6.75	−22.42	−1.76	0.772
6400	150.0	0.14	0.26	0.9	0.92	1.0	5.87	3.58	3.19	2.62	−0.77	3.13	−0.94	3.0	1.695
1516	500.0	0.01	0.05	0.64	0.77	1.0	10.98	6.91	7.27	7.38	1.23	2.2	3.0	−1.39	0.632
2273	500.0	0.01	0.05	0.52	0.68	1.0	4.17	2.79	3.12	3.14	11.13	7.02	18.98	2.53	1.395
2352	500.1	0.01	0.06	0.49	0.77	1.0	5.43	4.24	10.9	7.56	120.3	44.74	146.18	269.93	1.412
2984	500.0	0.01	0.05	0.41	0.71	1.0	6.67	3.97	4.02	3.63	−0.67	2.87	−1.01	−4.23	0.645
6340	500.0	0.05	0.09	0.56	0.79	1.0	8.28	4.23	4.02	3.48	6.66	1.85	10.99	−1.15	0.718

Notes.
[a] Convolved (using images convolved to the F2100W scale of 0.″67) photometry from H. Hassani et al. (2023) for clusters in the training set, as defined in Section 2.2 and Table 1.
[b] Star Cluster ID # from D. Maschmann et al. (2024).
[c] Adopted age as discussed in Section 2.3. The values with "0.1" attached are the outliers discussed in Section 2.5.
[d] The 0.814 flux in μJanskys can be used to convert the relative flux values in this table to absolute values.

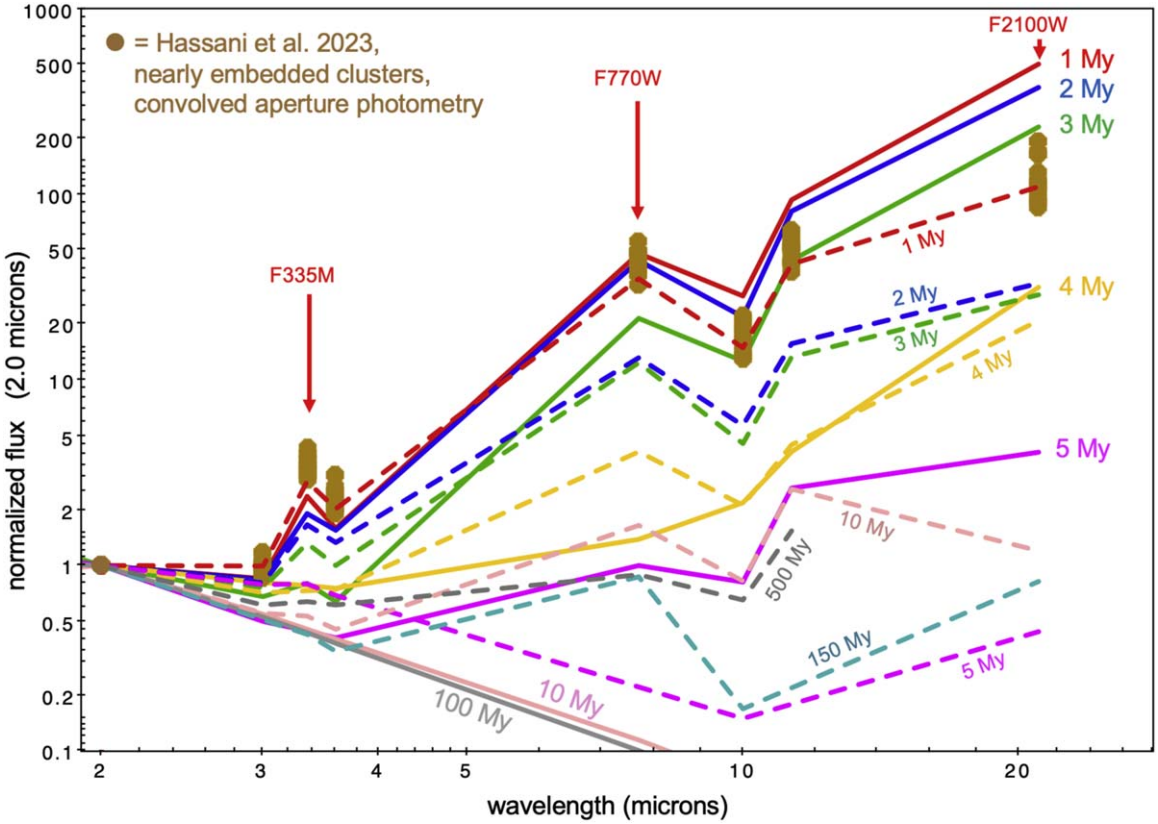

Figure 15. Similar to the bottom panel of Figure 10, but with templates derived from aperture photometry using images convolved to the size of the F2100W aperture (i.e., 0.″67) included as color-coded dashed lines. The brown points are from 12 nearly embedded cluster candidates from H. Hassani et al. (2023), as discussed in Section 3.2, and are most consistent with the 1 Myr convolved-aperture template (i.e., the red dashed line). Hence, the nearly embedded cluster candidates from the Hassani sample appear to be slightly younger than most of our optically selected clusters.

the apertures overplotted in the first panels of Figures 8 and 9). The case is less clear for 4 Myr in Figure 15, probably due to the increased noise from the patchy and erratic bubble structure. For ages of 5 Myr and older, the MIRI flux is essentially noise, as was the case in Figure 7.

ORCID iDs

Bradley C. Whitmore https://orcid.org/0000-0002-3784-7032
Rupali Chandar https://orcid.org/0000-0003-0085-4623
Janice C. Lee https://orcid.org/0000-0002-2278-9407
Kiana F. Henny https://orcid.org/0000-0001-7448-1749
M. Jimena Rodríguez https://orcid.org/0000-0002-0579-6613
Dalya Baron https://orcid.org/0000-0003-4974-3481
F. Bigiel https://orcid.org/0000-0003-0166-9745
Médéric Boquien https://orcid.org/0000-0003-0946-6176
Mélanie Chevance https://orcid.org/0000-0002-5635-5180
Ryan Chown https://orcid.org/0000-0001-8241-7704
Daniel A. Dale https://orcid.org/0000-0002-5782-9093
Kathryn Grasha https://orcid.org/0000-0002-3247-5321
Simon C. O. Glover https://orcid.org/0000-0001-6708-1317
Oleg Gnedin https://orcid.org/0000-0001-9852-9954
Hamid Hassani https://orcid.org/0000-0002-8806-6308
Remy Indebetouw https://orcid.org/0000-0002-4663-6827
Anand Utsav Kapoor https://orcid.org/0000-0002-5187-1725
Kirsten L. Larson https://orcid.org/0000-0003-3917-6460
Adam K. Leroy https://orcid.org/0000-0002-2545-1700
Daniel Maschmann https://orcid.org/0000-0001-6038-9511
Fabian Scheuermann https://orcid.org/0000-0003-2707-4678
Jessica Sutter https://orcid.org/0000-0002-9183-8102
Eva Schinnerer https://orcid.org/0000-0002-3933-7677
Sumit K. Sarbadhicary https://orcid.org/0000-0002-4781-7291
David A. Thilker https://orcid.org/0000-0002-8528-7340
Thomas G. Williams https://orcid.org/0000-0002-0012-2142
Aida Wofford https://orcid.org/0000-0001-8289-3428

References

Adamo, A., Ryon, J. E., Messa, M., et al. 2017, ApJ, 841, 131
Anand, G. S., Lee, J. C., Van Dyk, S. D., et al. 2021, MNRAS, 501, 3621
Anders, P., Bissantz, N., Fritze-v. Alvensleben, U., & de Grijs, R. 2004, MNRAS, 347, 196
Barnes, A. T., Chandar, R., Kreckel, K., et al. 2022, A&A, 662, L6
Baron, D., Sandstrom, K. M., Rosolowsky, E., et al. 2024, ApJ, 968, 24
Bastian, N., Konstantopoulos, I. S., Trancho, G., et al. 2012, A&A, 541, A25
Belfiore, F., Santoro, F., Groves, B., et al. 2022, A&A, 659, A26
Boquien, M., Burgarella, D., Roehlly, Y., et al. 2019, A&A, 622, A103
Brown, G., & Gnedin, O. Y. 2022, MNRAS, 514, 280
Bruzual, G., & Charlot, S. 2003, MNRAS, 344, 1000
Calzetti, D., Lee, J. C., Sabbi, E., et al. 2015, AJ, 149, 51
Chandar, R., Barnes, A. T., Thilker, D. A., et al. 2025, AJ, 169, 150
Chandar, R., Fall, S. M., & Whitmore, B. C. 2010, ApJ, 711, 1263
Chandar, R., Whitmore, B. C., Dinino, D., et al. 2016, ApJ, 824, 71
Chastenet, J., Sutter, J., Sandstrom, K., et al. 2023, ApJL, 944, L11
Chevance, M., Kruijssen, J. M. D., Hygate, A. P. S., et al. 2020, MNRAS, 493, 2872
Churchwell, E., Povich, M. S., Allen, D., et al. 2006, ApJ, 649, 759

Crowther, P. A., & Castro, N. 2024, MNRAS, 527, 9023
De Marchi, G., Paresce, F., Panagia, N., et al. 2011, ApJ, 739, 27
Deger, S., Lee, J. C., Whitmore, B. C., et al. 2022, MNRAS, 510, 32
Desert, F. X., Boulanger, F., & Puget, J. L. 1990, A&A, 237, 215
Draine, B. T. 2003, ARA&A, 41, 241
Draine, B. T., Dale, D. A., Bendo, G., et al. 2007, ApJ, 663, 866
Draine, B. T., Li, A., Hensley, B. S., et al. 2021, ApJ, 917, 3
Egorov, O. V., Kreckel, K., Sandstrom, K. M., et al. 2023, ApJL, 944, L16
Fahrion, K., & De Marchi, G. 2024, A&A, 681, A20
Floyd, M., Chandar, R., Whitmore, B. C., et al. 2024, AJ, 167, 95
Fouesneau, M., & Lançon, A. 2010, A&A, 521, A22
Fouesneau, M., Lançon, A., Chandar, R., & Whitmore, B. C. 2012, ApJ, 750, 60
Gaia Collaboration, Prusti, T., de Bruijne, J. H. J., et al. 2016, A&A, 595, A1
Grasha, K., Calzetti, D., Adamo, A., et al. 2019, MNRAS, 483, 4707
Grasha, K., Calzetti, D., Bittle, L., et al. 2018, MNRAS, 481, 1016
Gregg, B., Calzetti, D., Adamo, A., et al. 2024, ApJ, 971, 115
Grudić, M. Y., Guszejnov, D., Hopkins, P. F., Offner, S. S. R., & Faucher-Giguère, C.-A. 2021, MNRAS, 506, 2199
Grudić, M. Y., Guszejnov, D., Offner, S. S. R., et al. 2022, MNRAS, 512, 216
Hannon, S., Lee, J. C., Whitmore, B. C., et al. 2019, MNRAS, 490, 4648
Hannon, S., Lee, J. C., Whitmore, B. C., et al. 2022, MNRAS, 512, 1294
Hannon, S., Whitmore, B. C., Lee, J. C., et al. 2023, MNRAS, 526, 2991
Hassani, H., Rosolowsky, E., Leroy, A. K., et al. 2023, ApJL, 944, L21
Henny, K. F., Dale, D. A., & Chandar, R. 2025, ApJ, submitted
Hensley, B. S., & Draine, B. T. 2023, ApJ, 948, 55
Hollyhead, K., Bastian, N., Adamo, A., et al. 2015, MNRAS, 449, 1106
Kapoor, A. U., Baes, M., van der Wel, A., et al. 2023, MNRAS, 526, 3871
Kawamura, A., Mizuno, Y., Minamidani, T., et al. 2009, ApJS, 184, 1
Kim, J., Chevance, M., Kruijssen, J. M. D., et al. 2022, MNRAS, 516, 3006
Kotulla, R., Fritze, U., Weilbacher, P., & Anders, P. 2009, MNRAS, 396, 462
Krumholz, M. R., Fumagalli, M., da Silva, R. L., Rendahl, T., & Parra, J. 2015, MNRAS, 452, 1447
Lee, J. C., Sandstrom, K. M., Leroy, A. K., et al. 2023, ApJL, 944, L17
Lee, J. C., Whitmore, B. C., Thilker, D. A., et al. 2022, ApJS, 258, 10
Leger, A., & Puget, J. L. 1984, A&A, 137, L5
Leitherer, C., Li, I.-H., Calzetti, D., & Heckman, T. M. 2002, ApJS, 140, 303
Leitherer, C., Schaerer, D., Goldader, J. D., et al. 1999, ApJS, 123, 3
Leroy, A. K., Sandstrom, K., Rosolowsky, E., et al. 2023, ApJL, 944, L9
Li, A. 2020, NatAs, 4, 339
Lin, Z., Calzetti, D., Kong, X., et al. 2020, ApJ, 896, 16
Madden, S. C., Galliano, F., Jones, A. P., & Sauvage, M. 2006, A&A, 446, 877
Mallory, K., Calzetti, D., & Lin, Z. 2022, ApJ, 933, 156
Maragkoudakis, A., Ivkovich, N., Peeters, E., et al. 2018, MNRAS, 481, 5370
Maschmann, D., Lee, J. C., Thilker, D. A., et al. 2024, ApJS, 273, 14
Matthews, A. M., Johnson, K. E., Whitmore, B. C., et al. 2018, ApJ, 862, 147
Messa, M., Calzetti, D., Adamo, A., et al. 2021, ApJ, 909, 121
Neugebauer, G., Habing, H. J., van Duinen, R., et al. 1984, ApJL, 278, L1
Oey, M. S., & García-Segura, G. 2004, ApJ, 613, 302
Pathak, D., Leroy, A. K., Thompson, T. A., et al. 2024, AJ, 167, 39
Pedrini, A., Adamo, A., Calzetti, D., et al. 2024, ApJ, 971, 32
Pellegrini, E. W., Rahner, D., Reissl, S., et al. 2020, MNRAS, 496, 339
Pilbratt, G. L., Riedinger, J. R., Passvogel, T., et al. 2010, A&A, 518, L1
Povich, M. S., Stone, J. M., Churchwell, E., et al. 2007, ApJ, 660, 346
Puget, J. L., & Leger, A. 1989, ARA&A, 27, 161
Relaño, M., & Kennicutt, R. C., Jr. 2009, ApJ, 699, 1125
Robitaille, T., Rice, T., Beaumont, C., et al., 2019 astrodendro: Astronomical Data Dendrogram Creator, Astrophysics Source Code Library, ascl:1907.016
Rodríguez, M., Lee, J. C., Indebetouw, R., et al. 2025, arXiv:2412.07862
Rodríguez, M. J., Lee, J. C., Whitmore, B. C., et al. 2023, ApJL, 944, L26
Sandstrom, K. M., Bolatto, A. D., Bot, C., et al. 2012, ApJ, 744, 20
Sandstrom, K. M., Chastenet, J., Sutter, J., et al. 2023, ApJL, 944, L7
Schinnerer, E., & Leroy, A. K. 2024, ARA&A, 62, 369
Sun, J., He, H., Batschkun, K., et al. 2024, ApJ, 967, 133
Sutter, J., Sandstrom, K., Chastenet, J., et al. 2024, ApJ, 971, 178
Teh, J. W., Grasha, K., Krumholz, M. R., et al. 2023, MNRAS, 524, 1191
Thilker, D., Lee, J. C., & Whitmore, B. C. 2025, ApJS, submitted
Thilker, D. A., Whitmore, B. C., Lee, J. C., et al. 2022, MNRAS, 509, 4094
Turner, J. A., Dale, D. A., Lee, J. C., et al. 2021, MNRAS, 502, 1366
Watkins, E. J., Kreckel, K., Groves, B., et al. 2023, A&A, 676, A67
Weaver, R., McCray, R., Castor, J., Shapiro, P., & Moore, R. 1977, ApJ, 218, 377
Wei, W., Huerta, E. A., Whitmore, B. C., et al. 2020, MNRAS, 493, 3178
Werner, M. W., Roellig, T. L., Low, F. J., et al. 2004, ApJS, 154, 1
Whitmore, B. C., Brogan, C., Chandar, R., et al. 2014, ApJ, 795, 156
Whitmore, B. C., Chandar, R., Kim, H., et al. 2011, ApJ, 729, 78
Whitmore, B. C., Chandar, R., Lee, J., et al. 2020, ApJ, 889, 154
Whitmore, B. C., Chandar, R., Lee, J. C., et al. 2023a, MNRAS, 520, 63
Whitmore, B. C., Chandar, R., Rodríguez, M. J., et al. 2023b, ApJL, 944, L14
Whitmore, B. C., Chandar, R., Schweizer, F., et al. 2010, AJ, 140, 75
Whitmore, B. C., Lee, J. C., Chandar, R., et al. 2021, MNRAS, 506, 5294
Whitmore, B. C., & Zhang, Q. 2002, AJ, 124, 1418
Williams, T. G., Lee, J. C., Larson, K. L., et al. 2024, ApJS, 273, 13
Wofford, A., Charlot, S., Bruzual, G., et al. 2016, MNRAS, 457, 4296
Worthey, G. 1994, ApJS, 95, 107
Zackrisson, E., Rydberg, C.-E., Schaerer, D., Östlin, G., & Tuli, M. 2011, ApJ, 740, 13